

# Modelling Cosmic Infrared Background with evolving galaxies

A.A. Ermash<sup>1</sup>  S.V. Pilipenko,<sup>1</sup>  V.N. Lukash,<sup>1</sup> 

<sup>1</sup>*AstroSpace Center of P.N. Lebedev Physical Institute of RAS, Russia, Moscow.*

Accepted XXX. Received YYY; in original form ZZZ

## ABSTRACT

Sensitivity of future far infrared space telescopes like Millimetron will be limited by a confusion noise created by distant galaxies. We construct a model of the Cosmic Infrared Background (CIB) aimed at exploration of methods of prediction and reducing the confusion noise. The model is based on a public available eGALICS simulation. For each simulated galaxy we construct a spectral energy distribution with the help of public GRASIL and CHE\_EVO codes. In this paper, in order to put our model in the context of current CIB investigations, we compare the outputs of the model: luminosity and mass functions, source counts as a function of flux and redshift, spectrum of the CIB, prediction of confusion limit, with the available observational data and with three other models: one is a well known "backwards evolution" model of Bethermin et al. 2011 and two others are based on a simple mass-luminosity (M-L) relation applied to simulated dark matter halo catalogues. We conclude that our model reproduces the observational data reasonably well. All four models show significant differences in the predictions of the distribution of sources on the flux-redshift plane, especially at high redshifts. The predicted confusion noise on the wavelengths 70–350 microns is consistent between models, while for 650–2000 microns there are significant differences and M-L models should not be used.

**Key words:** submillimetre: diffuse background – galaxies: statistics – galaxies: evolution

## 1 INTRODUCTION

Our Universe is filled with background radiation in the full range of electromagnetic spectrum. Due to huge progress in the Far Infra Red (FIR) astronomy in the past few decades, the Cosmic Infrared Background (CIB) is getting more and more attention. This background is comprised by the radiation of submillimeter galaxies which have maximum of their spectral energy distribution (SED) at about 100  $\mu\text{m}$  in the galaxy's rest frame due to large amounts of dust produced by active star formation. The density of submillimeter galaxies on the sky is so high, that for FIR telescopes with apertures less than few tens of meters a fraction of these galaxies will be unresolved, i.e. there is a problem of confusion which affects sensitivity of FIR telescopes (Dole et al. 2004).

The sensitivity of future space FIR missions such as Millimetron (Smirnov et al. 2012; Kardashev et al. 2014), Callisto, OST in the mode of wide band photometry will be limited by confusion. Several approaches have been proposed how the sensitivity can be improved beyond the confusion limit. Optical data can be used to get positions of possible submillimeter sources and then to model their approximate SEDs and subtract their contribution from FIR observations (Safarzadeh et al. 2014). Another opportunity is to use submm spectral lines which can give redshifts and other properties

of unresolved galaxies. This information can be used to decrease the confusion limit by an order of magnitude (Raymond et al. 2010). A modern multi-band source extraction software can use information from the shortest wavelengths (where the resolution is the best) in order to better decompose crowded picture at longer wavelengths. This is implemented in, e.g., GETSOURCES, GETFILAMENTS and GETIMAGES (Men'shchikov et al. 2012; Men'shchikov 2013, 2017).

Estimating the usefulness of these methods can be done by simulating observations with future instruments. Existing observations cannot be used for this purpose: the data from space observatories (Herschel, Spitzer, Akari) suffer from the relatively low angular resolution and sensitivity in comparison with future observatories. The observations of ALMA have high enough angular resolution and sensitivity, but they have a very limited area on the sky and will not cover the shortest wavelengths,  $\lambda < 300 \mu\text{m}$ . Thus, we need an accurate model, which will predict the distribution of sources with different spectra on the sky, over redshifts and luminosities which can be probed by future space missions. Building such a model and testing it against existing observational data and other models is the goal of this paper. In next papers we plan to use this model to test various approaches in beating the confusion limit.

There is already a large number of papers in which various models of the CIB are developed. They can be divided into three groups:

backwards evolution;

\* E-mail: aermash@gmail.com  
 † E-mail: spilipenko@asc.rssi.ru  
 ‡ E-mail: lukash@asc.rssi.ru

semi-analytical models;  
semi-numerical models.

In the first group of models the population of galaxies is described by a luminosity function (LF) or a series of luminosity functions of several populations of galaxies with different spectra. The LFs are evolving with redshift, and this evolution is parameterized by some simple mathematical law. The parameters of the evolution are found by fitting the model to all existing observational data, including source counts and measurements of LFs. Since the LF data at low redshifts is the most complete, this data defines the shape of the LF which is then evolved backwards in time to fit other data, such as source counts. This type of models has advantage of very accurate reproduction of the observational data. Due to this advantage we use the backwards evolution model by [Béthermin et al. \(2011\)](#) as a reference for comparison with our own model. The details of this model are discussed in Section 3 in more detail. On the other hand backwards evolution models may lack predictive power in the range not probed by observations. Such models also usually do not take into account the large scale structure of the Universe and the hierarchical clustering of matter.

Models of this type were developed in many papers, e.g. [Béthermin et al. \(2012b\)](#); [Franceschini et al. \(2010\)](#); [Gruppioni et al. \(2011\)](#); [Jeong et al. \(2006\)](#); [Rahmati & van der Werf \(2011\)](#); [Rowan-Robinson \(2009\)](#); [Valiante et al. \(2009\)](#); [Weinmann et al. \(2012\)](#); [Lagache et al. \(2003\)](#); [Dole et al. \(2003\)](#); [Domínguez et al. \(2011\)](#); [Marsden et al. \(2011\)](#); [Le Borgne et al. \(2009\)](#); [Chary & Elbaz \(2001\)](#); [Pearson \(2001\)](#); [Roche & Eales \(1999\)](#); [Takeuchi et al. \(2001\)](#); [Tan et al. \(1999\)](#); [Wilman et al. \(2008, 2010\)](#). They differ by the number of galaxy populations used (2–5 populations) and by the main function which describes the evolution. In particular, in [Rahmati & van der Werf \(2011\)](#) a color – luminosity function is used instead of LF, while [Béthermin et al. \(2012b\)](#) is based on the evolution of the specific star formation rate.

The second group is represented by semi-analytical models, which are based on the evolution of dark matter (DM) haloes, which is described by the halo mass function. Sometimes the spatial distribution of haloes is also taken into account by using the power spectrum of halo number density perturbations. Both the mass function and power spectrum can be computed by numerical integration, without running N-body simulations. Then haloes with given mass  $M$  are assigned luminosity using mass-to-light relation, and quantities of interest such as source counts, LFs, can be easily computed by assuming some spectral energy distribution. Examples of such models are found in [Guiderdoni et al. \(1998\)](#); [Devriendt & Guiderdoni \(2000\)](#); [Bouché et al. \(2010\)](#); [Conroy & Wechsler \(2009\)](#); [Granato et al. \(2004\)](#); [Hopkins et al. \(2008a,b\)](#); [Lacey et al. \(2010\)](#); [Cole et al. \(2000\)](#); [Somerville et al. \(2008\)](#); [Younger & Hopkins \(2011\)](#); [Wang & Biermann \(2000\)](#); [Wang \(2002\)](#).

The third group of semi-numerical models differs from semi-analytical ones by the usage of results of N-body cosmological simulations, from which halo catalogs are extracted. Halos are then populated with galaxies basing on their merging and accretion history. This makes semi-numerical models the most accurate in reproducing the large scale structure of the Universe. Examples of such models are [Cattaneo et al. \(2005, 2006\)](#); [Cousin et al. \(2015a,b\)](#); [Croton et al. \(2006\)](#); [Guo et al. \(2011\)](#); [Monaco et al. \(2007\)](#); [Henriques et al. \(2013\)](#); [Hopkins et al. \(2010\)](#).

One should note that classification of CIB models presented here is simplified, and there exist models which incorporate features of different types of models. Earlier we have developed a simple semi-numerical model in which simulated haloes were assigned lu-

minosities according to a mass-luminosity relation [Pilipenko et al. \(2017\)](#). We have found the parameters of the mass-luminosity relation by fitting observed source number counts. The model reproduced source counts with high enough precision in the range 100–2000 microns. It also has reproduced the angular power spectrum of CIB observed by Herschel ([Viero et al. 2013](#)). However, our model used a single SED for all galaxies, thus it failed to reproduce galaxy properties at shorter wavelengths.

In this paper we construct a model of extragalactic background light (EBL) using the eGALICS simulation from Cousin et al. (2015a) and Cousin et al. (2015b). The public available eGALICS data contains dark matter halo parameters as well as properties of stellar and gaseous components built using a semi-numerical approach. We create a SED library with the GRASIL and CHE\_EVO program codes (Silva et al. 1998) and assign each model galaxy its individual SED. We distribute galaxies in a cone of a model survey and analyse properties of this survey. The main advantages of our CIB model in comparison with many published models of submillimeter galaxies are 1) the usage of N-body simulations which guarantees the most precise large scale structure, hierarchical clustering and dark matter halo parameters, 2) the absence of free parameters tuned to fit the observations and 3) taking into account the complex evolution of SEDs of galaxies.

The paper is organized as follows: in Section 2 we give the parameters of Millimetron space observatory since our ultimate goal is to develop methods to beat the confusion limit, which can be used for observations with Millimetron. Thus, Millimetron defines the requirements for our model. In section 3 we describe the models that we consider in this paper, the original data and methods used. In Section 4 we give and discuss our results: mass and luminosity functions are given in Section 4.1, integral and differential source counts are presented in Section 4.2, the 2D plots of contribution from objects with different fluxes at different redshifts to the number counts can be found in section 4.3. The spectrum of the CIB and contribution of sources on different redshifts and luminosities is given in Section 4.4, the confusion noise is computed in Section 4.5. A summary of our work is given in Section 5. In the Appendix A we discuss the predicted optical number counts in SDSS bands.

## 2 MILLIMETRON SPACE MISSION

The primary goal of this study is to create a model that will allow us to gauge CIB parameters for the planning Millimetron space mission. The detailed characteristics of the telescope and scientific payload can be found in [Kardashev \(2017\)](#); [Kardashev et al. \(2014\)](#); [Smirnov et al. \(2012\)](#) and on the official website of the project<sup>1</sup>. Below we describe the parameters that are vital for this work.

The Millimetron space mission will have a 10-m diameter primary mirror that will be actively cooled to the temperature 4.5 K. The spacecraft will be launched to the orbit near L2 point of the Earth-Sun system. Photometric observations will be carried out with LACS (Long wave Array Camera Spectrometer) and SACS (Short wave Array Camera Spectrometer) instruments. Their wavebands are listed in Table 1

Short wave matrix spectrometer (SACS) will consist of two main parts – the matrix photometer operating in the whole frequency range, which is divided into several subbands by dichroic beam splitter, and a matrix spectrome-

<sup>1</sup> millimetron.ru

**Table 1.** LACS and SACS detector parameters of the Millimetron Mission. Details see in text.

	Band 1	Band 2	Band 3	Band 4
Long wave Array Camera Spectrometer				
Wavelength(μm)	3000–1500	1500–850	850–450	450–300
FWHM (arcsec)	42	22	12	7.5
Short wave Array Camera Spectrometer				
Wavelength(μm)	50–90	90–160	160–300	300–450
FWHM (arcsec)	1–2	2–4	4–6	6–10

**Table 2.** Past, present day and currently under development space telescopes. In this table we cite the general parameters of the following instruments: Spitzer (Rieke et al. (2004)) with MIPS – The Multiband Imaging Photometer. Herschel with PACS and SPIRE. APEX LABOCA – Atacama Pathfinder EXperiment the Large Apex BOlometer CAmera (Siringo et al. 2009), SABOCA – The Submillimetre APEX Bolometer CAmera (Siringo et al. 2010). IRAS – Infrared Astronomical Satellite (Beichman et al. 1988). Akari (Murakami et al. 2007). AzTEC camera (Wilson et al. 2008) that was initially used with 15-m James Clerk Maxwell Telescope (JCMT) and later with 10-m Atacama Submillimeter Telescope Experiment (ASTE) and 50-m Large Millimeter Telescope(LMT).

Telescope	Detector	Wavelengths
Spitzer, 0.85-m	MIPS	24, 70, 160 μm
Herschel, 3.29-m	PACS	130–210, 60–90
	PACS	90–130 μm
	SPIRE	250, 350, 500 μm
APEX 12-m	LABOCA	870 μm
	SABOCA	350 μm
IRAS 57-cm		12, 25, 60 and 100 μm
Akari 68.5-cm	N60	65 μm
	Wide-S	90 μm
	Wide-L	140 μm
	N160	160 μm
James Clerk	SCUBA 1	450, 850 μm
Maxwell Telescope	SCUBA 2	450, 850 μm
(JCMT) 15m, ground		
JCMT, ASTE, LMT	AzTEC	1100 μm

ter, the spectral resolution of which will be determined by the input optical filter. A similar approach was used in the PACS receiver (<http://www.cosmos.esa.int/web/herschel/science-instruments>), successfully operated as part of the Herschel Space Observatory, which, undoubtedly, will be used in the development of short wave matrix spectrometer for the Millimetron observatory.

LACS is similar to the SPIRE receiver (<http://www.cosmos.esa.int/web/herschel/science-instruments>) that successfully operated as a part of the Herschel Space Observatory. Simultaneously, this receiver will be optimized for precise measurement of Syunaev-Zeldovich effect. The spectrometer whole frequency range from 100 GHz to 1 THz will be divided into 4 sub-bands. See Table 1.

### 3 DATA USED

In this study we utilize the data from the following three sources. The first is the model created by the authors of this study, previous version of which was described in detail in Pilipenko et al. (2017). In this paper we refer to it as P2017.

As a second model we considered the IRGAL project and the

model presented by Béthermin et al. (2011). Here we refer to it as BM, the Béthermin backward evolution Model.

Finally, we used the eGALICS model. The simulation is described in copious details in Cousin et al. (2015a) and Cousin et al. (2015b).

Our models of the EBL are based on different cosmological simulations and thus imply different cosmological parameters. For the P2017 model the Cosmology was as following:  $\Omega_{\Lambda 0} = 0.692885$ ,  $\Omega_{m0} = 0.307115$ ,  $H_0 = 67.77 \text{ km s}^{-1} \text{ Mpc}^{-1}$  Klypin et al. (2016). In the BM model the cosmology was:  $\Omega_{\Lambda 0} = 0.734$ ,  $\Omega_{m0} = 0.266$ ,  $H_0 = 71.0 \text{ km s}^{-1} \text{ Mpc}^{-1}$  Larson et al. (2011). And the eGALICS simulation was based on the WMAP 3-yr cosmology:  $\Omega_{\Lambda 0} = 0.76$ ,  $\Omega_{m0} = 0.24$ ,  $H_0 = 73 \text{ km s}^{-1} \text{ Mpc}^{-1}$ . As will be shown below, such differences do not greatly affect the results of interest.

For all the calculations the Python 2.7 language was used.

### 3.1 P2017 model

Let us briefly describe the approach used in creation of the model that was previously published in Pilipenko et al. (2017). Using the COSMOSIM database we have extracted all available redshift cuts in the Small Multidark Planck Klypin et al. (2016) numerical model. The size of the cube was  $40 \text{ Mpc h}^{-1}$  and the angle of the cone was set to  $1^\circ \times 1^\circ$ .

The orientation of the axis of the cone was set such that any part of the cube contributes to the cone only once. Minimum and maximum redshifts were set to  $z_{min} = 0.30$  and  $z_{max} = 6.19$ . Minimum and maximum mass of a DM halo in the simulation was, respectively,  $M_{min} = 3 \times 10^{10} M_\odot$ ,  $M_{max} = 2.56 \times 10^{14} M_\odot$ . The total amount of haloes  $N = 1285307$ . Lensing was accounted for with the assumption of a point lens model. Magnification coefficient in such a case is (see, e.g. Schneider et al. (1992))

$$\mu(M_L, D_L, D_S, \beta) = \frac{\tilde{\beta}^2 + 2}{\tilde{\beta}\sqrt{\tilde{\beta}^2 + 4}} \quad (1)$$

where

$$\tilde{\beta} = \frac{\beta}{\alpha_0} \quad (2)$$

$\beta$  – angular distance between lens and the source  $\alpha_0$  – characteristic angular distance which in turn depends on redshift of the source  $z_S$  and redshift of the lens  $z_L$ . Equation for calculation of  $\alpha_0$  can be found in the same paper Schneider et al. (1992):

$$\alpha_0 = \sqrt{\frac{4GM_L}{c^2}} \frac{D_{LS}}{D_S D_L (1+z_L)} \quad (3)$$

$D_L$  and  $D_S$  – comoving distance between the observer and the lens and from the observer and the source, respectively.  $D_{LS}$  – comoving distance between the lens and the source,  $z_L$  – redshift of the lens,  $c$  – speed of light,  $G$  – gravitational constant. We only considered lensed objects with magnification coefficient greater than 2.

We utilized the the following frequently used equation as a  $M - L$  ratio:

$$L(M, z) = L_0 (1+z)^\eta \log(M) \exp\left(-\frac{(\log(M) - \log(M_0))^2}{2\sigma_L^2}\right) \quad (4)$$

The parameters were as following:  $\log(M_0) = 12.6$ ,  $\sigma_L^2 = 0.15$ ,  $\eta = 3.16$  when  $z < 2$  and  $\eta = 0$  when  $z > 2$ ,  $L_0 = 5 \times 10^9 L_\odot$  for the IR luminosity in the wavelength range of 8–1000 μm. Averaged spectra of galaxies were taken from Michałowski et al. (2010).

### 3.2 IRGAL

In order to compare predictions of fundamentally different approaches we also performed calculations following the prescriptions of Béthermin et al. (2011) (the BM model). Let us shortly describe here their approach. Two populations of objects, namely ‘normal galaxies’ and ‘starforming galaxies’ are considered. Thus, two spectra were utilized. It should be noted that the shape of the latter depends on luminosity. The luminosity function has the following shape:

$$\Phi(L_{IR}) = \Phi^* \times \left( \frac{L_{IR}}{L^*} \right)^{1-\alpha} \times \exp \left[ -\frac{1}{2\sigma^2} \log_2 \left( 1 + \frac{L_{IR}}{L^*} \right) \right] \quad (5)$$

where  $\Phi^*$  is the constant of normalization,  $L^*$  characteristic luminosity of the break,  $\sigma = 0.406$  characterizes the bright end of the luminosity function. The redshift evolution is set in the following way:  $L^* \propto (1+z)^{r_L}$ ,  $\Phi^* \propto (1+z)^{r_\phi}$ , where  $r_L$  and  $r_\phi$  are the parameters characterizing the evolution. These coefficients depend on the redshift. They change twice, at redshifts  $z_{break,1} = 0.879$  and  $z_{break,2} = 2.0$ . For these three intervals the numerical values are as following:  $r_{L^*,l_z} = 2.931$ ,  $r_{\Phi^*,l_z} = 0.774$ ,  $r_{L^*,m_z} = 4.737$ ,  $r_{\Phi^*,m_z} = -6.246$ ,  $r_{L^*,h_z} = 0.145$ ,  $r_{\Phi^*,h_z} = -0.919$ . Where  $l_z$  means ‘low  $z$ ’,  $m_z$  – ‘intermediate redshifts’ and  $h_z$  – ‘high redshifts’ respectively.

The fraction of ‘starforming galaxies’ is expressed in the following way:

$$\frac{\Phi_{starburst}}{\Phi} = \frac{1 + \tanh[\log_{10}(L_{IR}/L_{pop})/\sigma_{pop}]}{2} \quad (6)$$

The parameter  $L_{pop} = 23.677 \times 10^{10} L_\odot$  corresponds to the luminosity at which the amounts of normal and starforming galaxies are the same, while  $\sigma_{pop} = 0.572$  characterizes the width of the transition between these two populations.

As a next step the grid in  $S_\nu$  and redshift  $z$  is created and  $L_{IR}(S_\nu, z, pop)$  and  $dL_{IR}/dS_\nu$  are calculated on it.

The counts of sources are calculated with the following formula:

$$\begin{aligned} \frac{dN}{dS_\nu d\Omega} &= \\ \sum_{pop} \int_0^\infty f_{pop}(L_{IR}) \frac{dN}{dL_{IR} dV} |L_{IR}(S_\nu, z, pop) \frac{dL_{IR}}{dS_\nu} \frac{dV}{dz d\Omega} dz &= \\ \sum_{pop} \int_0^\infty \frac{dN}{dS_\nu dz d\Omega} dz & \end{aligned} \quad (7)$$

where  $dN/dS_\nu/d\Omega$  is the number of objects per flux unit per unit solid angle,  $f_{pop}(L_{IR})$  is a fraction of galaxies of certain population defined by equation 6,  $dN/dL_{IR}/dV$  is derived from equation 5 the following way

$$\frac{dN}{dL_{IR} dV} = \frac{dN}{d \log_{10}(L_{IR}) L_{IR} \log(10) dV} = \frac{\Phi(L_{IR})}{L_{IR} \log(10)} \quad (8)$$

The values of  $dN/dS_\nu/dz/d\Omega$  are calculated on the grid and saved for further use.

As can be derived from Perrotta et al. (2001) and Perrotta et al. (2002), the probability of lensing with multiplication factor greater than  $\mu$  at redshift  $z_s$  can be written in the following form:

$$\begin{aligned} P(\mu, z_s) &= \frac{(1+z_s)^2}{4\pi r^2(z_s)} \int_0^{z_s} dz \frac{dV}{dz} (1+z)^3 \\ &\times \int dM \sigma(\mu, z, z_s, M) n_c(z, M) \end{aligned} \quad (9)$$

In this equation  $r(z)$  is a comoving distance to the redshift  $z$ ,  $dV/dz$  is a volume element,  $n_c(z, M)$  – comoving lens density. If we use  $n(z, M) \equiv (1+z)^3 n_c(z, M)$  instead of  $n_c(z, M)$ , then the equation 9 takes the similar form of equation 13 from Béthermin et al. (2011).

Following Béthermin et al. (2011) we utilized mass function from Reed et al. (2007). The source code that was originally written in Fortran language was modified and used with the f2py utility – Fortran to Python interface generator.

The cross-section of lensing with magnification factor greater than  $\mu_{tot} > \mu$  is expressed with the following formula (Perrotta et al. (2001) and Perrotta et al. (2002)):

$$\sigma(\mu_{tot} > \mu) = \frac{4\pi \hat{\alpha}^2 D_{ds}^2}{\mu^2} \quad (10)$$

where  $\hat{\alpha}$  is expressed the following way.

$$\hat{\alpha} = 4\pi \frac{\sigma_v^2}{c^2} \quad (11)$$

In equations 10 and 11:  $\sigma_v$  – halo velocity dispersion,  $D_{ds}$  – angular diameter distance between the lens and the object.

For a virialized halo the ratio between collisionless matter and the gas temperature is expressed as:

$$\beta = \frac{\mu m_p \sigma^2}{kT} \quad (12)$$

where  $\mu$  – molecular mass of the interstellar gas,  $m_p$  is the proton mass,  $k$  is the Boltzmann constant,  $T$  is the temperature (see, e.g., Bryan & Norman (1998)). The molecular mass of the interstellar gas  $\mu = 0.6$  was taken from Rosati et al. (2002). The following equation for temperature was used (Ilić et al. 2015):

$$T = A_{TM} (h M_v)^{2/3} \left( \frac{\Omega_m \Delta(\Omega_m, z)}{178} \right)^{1/3} (1+z)^{1+\alpha_{TM}} \quad (13)$$

In this equation  $A_{TM} = 6.29$  is the normalization constant,  $h$  is the dimensionless Hubble constant,  $M_v$  is the virial mass in units  $10^{15} M_\odot$ ,  $\Omega_m = \Omega_{m0}(1+z)^3/E^2(z)$ , and  $E(z) = H(z)/H_0 = [\Omega_{m0}(1+z)^3 + \Omega_{R0}(1+z)^2 + \Omega_{\Lambda0}]^{1/2}$ . Also  $\Delta(z) = 18\pi^2 + 82x - 39x^2$ , where  $x = \Omega_m - 1$ . See, e.g. Bryan & Norman (1998).

We utilized the approach in calculations described in Béthermin et al. (2011). Firstly matrices with coefficients corresponding to the lensing probability are calculated. As the next step matrices containing the source counts (axes are  $S_\nu$  and  $z$ ) are multiplied with the lensing matrices.

### 3.3 eGALICS data

In order to create a model of extragalactic background based on the simulations of the barionic matter we made use of the data of the eGALICS project. The detailed description of this model can be found in the following two papers: Cousin et al. (2015a) and Cousin et al. (2015b). Creators of the simulation call it ‘Semianalytical’. As the first step the simulation of the dark matter with the following parameters was created. Cosmology – WMAP-3yr, where  $\Omega_m = 0.24$ ,  $\Omega_\Lambda = 0.76$ ,  $f_b = 0.16$ ,  $h = 0.73$ . Volume of the simulation  $(100h^{-1})^3 \approx 150 Mpc^3$ , number of particles  $1024^3$ , each with mass  $m_p = 8.593 \times 10^7 M_\odot$ , minimal halo mass  $M_h^{min} = 1.707 \times 10^9 M_\odot$ . Then authors of the model add barionic matter taking into account the formation of discs, pseudobulges, supernova feedback, AGN, hot halo, cooling processes etc. One of the key new elements of the model considered is the cold non-starforming gas reservoir.

The first step one must take to create the background model

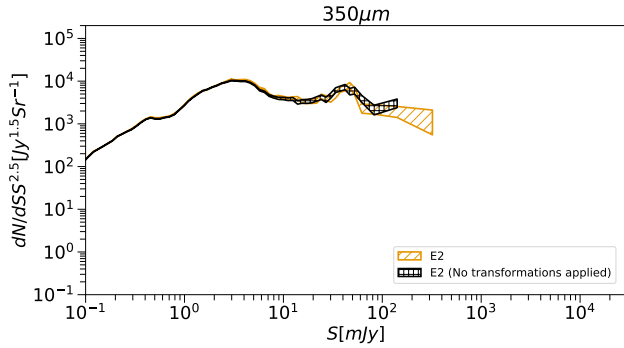


**Figure 1.** Differential number counts at  $\lambda = 350\mu\text{m}$ . Two hatched areas show predictions of the E2 model with and without transformations applied to the model cubes. Details see in text.

from this simulation is to create a cone. If one creates a large cone from simulation with quite modest cube size a certain problem arises. The same part of the cube is included multiple times in the cone. Large scale structure evolves rather slowly, thus the repeating elements create the effect of perspective. This effect is illustrated on the left panel of the Fig. 3. Original solution to this problem was proposed in Blaizot et al. (2005). During the process of the creation of the cone each cube is affected by the following transformations independently on each axis: shift with random distance, rotation to  $\pi/2$ ,  $\pi$  or  $-\pi/2$ , reflection along selected axis.

The result of such transformation is shown on Fig. 3, right panel. As should be expected, the repeating structures are absent. The presence of such structures affects not only the outlook of the model map of the sky and the angular correlation function, but also the source counts. In order to illustrate this the angular correlation functions at the  $\lambda = 350\mu\text{m}$  wavelength are shown on the Fig. 2 and differential number counts for the two cones are shown on Fig. 1. The elements of the first cone were affected by the aforementioned transformations while the elements of the second were not. Correlation function was calculated for objects with the flux within the interval  $\log_{10}(S_{350\mu\text{m}}[\text{mJy}]) = 0.0^{+0.1}_{-0.1}$ . In order to calculate the two-point correlation function the Vanderplas et al. (2012) astronomical package was used. The method of assessing the correlation function is the one described in Landy & Szalay (1993):

$$\omega(\theta) = \frac{DD - 2DR + RR}{RR} \quad (14)$$

In this equation  $DD$  is the number of pairs in the simulation,  $RR$  is the number of pairs in the random sample,  $DR$  is the number of pairs between the simulation and the random sample.

As can be seen from the plot, the differences are quite severe. Correlation function of the map obtained without transformations shows excess clusterisation on low angular scales. For differential number counts the differences are significant on large fluxes. That effect can be easily explained. There are more objects with lower fluxes, and due to averaging the effect of real spatial distribution is decreased.

We used eGALICS data to create two models of EBL. The first is a simple one based on a  $M-L$  relation, and the second took properties of baryonic matter into account. Comparison of these two models will show the importance of taking the full physics into account.

At first let us consider a simple model of the EBL. We used information about dark matter halo mass, mass–luminosity relation

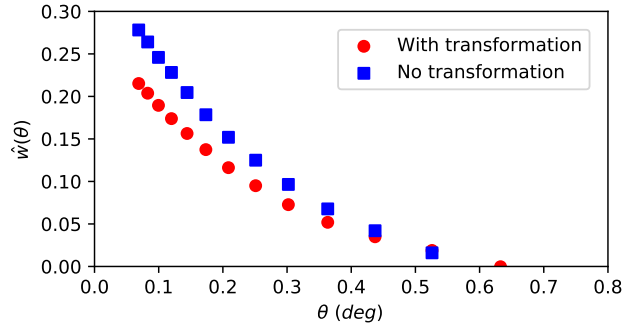


**Figure 2.** Correlation functions of model simulations. Circle markers – the transformations were applied to cubes of the simulation. Square markers – no transformations were applied to the cubes. Error bars are the same size as markers. Details see in text.

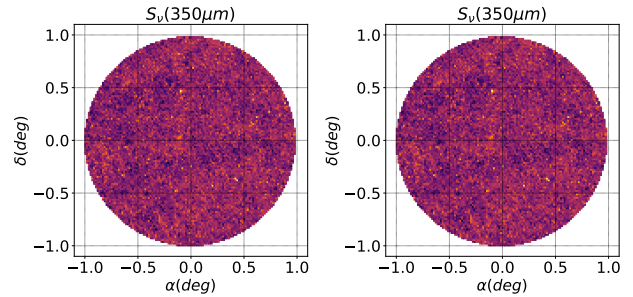


**Figure 3.** Model maps of the E2 model. Wavelength  $350\mu\text{m}$ , pixel size is 1 angular minute. Left panel: maps obtained without applying any transformation to the cubes. Repeated structures can be clearly seen. Right panel: transformations described above were applied to individual cubes. The repeated structures can not be detected visually.

and a simple model spectrum. We refer to this model as E1. These ingredients are sufficient to calculate fluxes. The  $M-L$  ratio was taken from Planck Collaboration et al. (2014):

$$L_{(1+z)\nu}(M, z) = L_0 \Phi(z) \Sigma(M, z) \Theta[(1+z)\nu] \quad (15)$$

where  $\Phi(z) = (1+z)^\delta$  and

$$\Sigma(M, z) = M \frac{1}{(2\pi\sigma_{L/M}^2)^{1/2}} e^{-(\log_{10}(M) - \log_{10}(M_{eff}))^2 / 2\sigma_{L/M}^2} \quad (16)$$

Parameters in this equation are, respectively:  $\delta = 3.6$ ,  $\sigma_{L/M}^2 = 0.5$   $\log_{10} M_{eff} = 12.6$  ( $M_{eff}$  is in units of  $M_\odot$ ),  $L_0 = 0.0135 L_\odot$ ,  $M_{min} = 1.0 \times 10^{10} M_\odot$ . First three parameters were adopted from Planck Collaboration et al. (2014), the latter two from Wu & Doré (2017). In case when  $M < M_{min}$  luminosity  $L = 0$ . If  $z > 2$  parameter  $\delta = 0$ .

We used the SED library of Chary & Elbaz (2001). The data is publicly available at the website: [http://david.elbaz3.free.fr/astro\\_codes/chary\\_elbaz.html](http://david.elbaz3.free.fr/astro_codes/chary_elbaz.html). The library consists of 105 spectra for the luminosity interval  $L = 2.73 \times 10^8 L_\odot - 3.53 \times 10^{13} L_\odot$ . As a simplistic first approximation such library allows reproduction of variety of types of galaxies if we imply simple dependence of their parameters on mass. But it should be noted that usage of such a library is only justified if we aim at creating a simplistic model for illustrative purposes. The reason is that this library was created for local galaxies on low redshifts. The fact that SEDs of galaxies change

with redshift was put under close consideration in numerous works. See for example the paper dedicated to the GRASIL code: [Silva et al. \(1998\)](#).

Plots of differential and integral number counts and of confusion noise criteria obtained by this simplified approach are shown at corresponding figures in sections 4.1–4.5.

On the plots of differential and integral number counts, luminosity and mass functions errors were Poissonian. Details see [Gehrels \(1986\)](#).

In order to obtain the results of interest from the eGALICS simulation we utilized the following approach. Hereafter we refer to this model as E2. Discs and bulges were treated independently due to the fact that in the simulation there is data available for them separately. We create a library of SEDs using the publicly available code GRASIL and CHE\_EVO ([Silva et al. 1998](#)). This code calculates spectral evolution of stellar systems taking dust effects into account.

For our purposes two libraries of SEDs were created, for discs and bulges respectively. The first one contained 16164 spectra, the second 7056 spectra. The grid of parameters is given in Table 3. Parameters that are not mentioned in Table 3 were left by default according to the recommendations of creators of the code.

For each object in the eGALICS cone with disc and/or bulge the closest model in the parameter space was found. The parameters were: age of the galaxy  $t_{gal}$ , stellar mass  $M_*$ , mass of gas  $M_{gas}$ , star formation rate and metallicity. For further processing we selected models which differ from the eGALICS object in stellar mass less than 0.1 dex. We also excluded model that are more than 5Gyr younger than the age of the Universe. The result of these operations is a model cone that contains three-dimensional coordinates of the objects and the identifier in the bulge and/or disc in the library.

As can be seen from the Table 3 in order to keep the calculation time reasonable, the step in each parameter should not be to small. In order to at least partly compensate the effects of the discrete step in each parameter we utilized the following approach. If  $i$  is a number of a model in the catalog then in the parameter space the distance between this model and the disc or bulge of the galaxy can be calculated the following way:

$$D_{i,gal}^2 = \sum_{k=1}^M (\log_{10}(P_{k,gal}) - \log_{10}(P_{k,i}))^2 \quad (17)$$

where  $P_{k,gal}$  –  $k$ -th bulge or disc parameter from the model cone,  $P_{k,i}$  –  $k$ -th parameter of the  $i$ -th bulge or disc from the library. If we consider the actual parameters, we can get:

$$\begin{aligned} D_{i,gal}^2 &= (\log_{10}(SFR_i) - \log_{10}(SFR_{gal}))^2 + \\ &(T_{*,i} - T_{*,gal})^2 + (\log_{10}(M_{gas,i}) - \log_{10}(M_{gas,gal}))^2 + \\ &(\log_{10}(R_i) - \log_{10}(R_{gal}))^2 \end{aligned} \quad (18)$$

where  $SFR_i, T_{*,i}, M_{gas,i}, R_i$  – for the  $i$ -th model from the catalogue, respectively: star formation rate, age, gas mass and radius.  $SFR_{gal}, T_{*,gal}, M_{gas,gal}, R_{gal}$  – the same parameters for the galaxy from the model cone. Here  $R$  means  $r_d$  for discs and  $r_c$  for bulges. We use  $T$  instead of  $\log_{10}(T)$ . This was done because in the most of equations governing the evolution of galaxies age contributes in exponential form:  $e^{kt}$ . Then for each disc or bulge we take weighted average of  $N$  models the following way:

$$\langle P_k \rangle = \frac{\sum_{i=1}^N X_i / D_{i,gal}^2}{\sum_{i=1}^N 1 / D_{i,gal}^2} \quad (19)$$

where summation is done for the  $N$  closest in distance  $D_{i,gal}$  ob-

jects.  $X$  is a quantity of interest, e.g. luminosity. In this work the value of  $N$  was set to 7.

During the next step of our work we had calculated the fluxes in the wavelengths of interest and integral IR luminosities. This is necessary to calculate differential and integral counts, luminosity function, etc.

It should be noted that for each bulge and disc we created 10 SEDs for the following inclination angles: 0°, 10°, ..., 90°. Each object was assigned a random inclination.

Contribution of the Active Galactic Nuclei was also taken into account. The eGALICS data provide bolometric luminosities of active nuclei in galaxies. Bolometric correction to the IR was taken from [Risaliti & Elvis \(2004\)](#) where it has the following form  $L_{IR} = 0.19L_{bol}$ . For simplicity's sake we used a single AGN SED template for AGN type 1 from [Lyu & Rieke \(2017\)](#). Their data reach only 2000 μm, but it is stated that on larger wavelengths the SED can be approximated by the black body SED with the temperature of 118 K.

In our calculations we also accounted for lensing. The method implied was analogous to the one described above and implemented in P2017.

In the following sections the results obtained with aforementioned model are described in detail.

## 4 RESULTS

### 4.1 Mass and luminosity functions

In every model the key element is a dark matter halo mass function and luminosity functions of galaxies. We plot them here in order to compare the models considered in this paper.

In the model of [Béthermin et al. \(2011\)](#) luminosity functions are set parametrically. With the use of e.g., ratio 15 it is possible to obtain mass function. Which in turn can be compared with the one used for lensing ([Reed et al. 2007](#)).

Fig. 4 shows these two mass functions along with the one from eGALICS model and from the model described in section 3.1. As can be seen, all mass functions show reasonable agreement. This is a principal thing because it advocates for basic agreement between models.

Let us consider the luminosity functions of the models. They are plotted on Fig. 5. For the eGALICS simulation two LFs are plotted. The first was simply obtained from the mass function with the ratio 15. The second one was calculated from the spectra of discs and bulges. For details see section 3.3. Unsmooth appearance of the luminosity functions derived from GRASIL SED library is due to the limited amount of model spectra.

At the redshift of  $z = 1$  models based on [Béthermin et al. \(2011\)](#), E1 and E2 show fair agreement. However, the P2017 model shows some discrepancy.

Towards higher redshifts the following trend can be clearly seen. Due to the lack of massive haloes on high redshifts LFs of E1 and P2017 show a drop off on large luminosities in comparison to the BM model. The fact that in these two model spectra of local galaxies were used as template also contributes to this tendency. In the E2 we used spectra of galaxies of various ages. So, as can be expected, the difference between the LF of these models and the others increases with redshift.

**Table 3.** Parameter grids for GRASIL and CHE\_EVO [Silva et al. \(1998\)](#). Detailed description of the meaning of each parameter can be found in the aforementioned paper of the authors of the code as well as on their website. Parameter names have superscripts on them, which mean: a – parameter of CHE\_EVO. b – GRASIL configuration file, section ‘MAIN’.

Parameter	Value	Unit	Comment
		DISCS	
t_fin <sup>a</sup>		Gyr	Up to this age chemical evolution is calculated. By default is set to tgal.
t_win <sup>a</sup>	20	Gyr	After $t_{win}$ the feed-back rate is multiplied by $f_{win}$ .
nu_sch <sup>a</sup>	[0.05, 0.5, 1.0, 2.0]		Efficiency of Schmidt law $v$ : $\Psi(t) = v M_g(t)^k$ .
tau_inf <sup>a</sup>	[2.0, 5.0, 9.0]	Gyr	Exponential infall time-scale.
f_win <sup>a</sup>	1		After $t_{win}$ the feed-back rate is multiplied by $f_{win}$ .
m_inf <sup>a</sup>	[1.0e5, 1.0e6, 1.0e7, 1.0e8]	$M_\odot$	Infall mass at $t_{inf}$ .
	[1.0e9, 1.0e10, 1.0e11]		
t_inf <sup>a</sup>	[13.0]	Gyr	See $m_{inf}$ .
mmolfraz <sup>b</sup>	[0.5]		Fraction of molecular over total gas mass.
rcloud <sup>b</sup>	[15.0]	pc	Radius (pc) of molecular clouds.
etastart <sup>b</sup>	[0.003, 0.08]	Gyr	Escape time-scale of young stars from MCs (Gyr).
idz <sup>b</sup>	1		This is a flag. If idz=0.0 dsug is simply the dust/gas mass ratio, if idz=1.0 then dsug becomes the proportionality factor between Z (metallicity) and dust/gas.
dsug <sup>b</sup>	0.45		See idz.
igeo <sup>b</sup>	2		Flag that sets the geometry of stars and gas. In this case the exponential profile was used.
rdstar=rddiff <sup>b</sup>	[3.000e-02, 9.587e-02, 3.064e-01 , 9.791e-01, 3.129e+00, 1.000e+01]	kpc	Scale lengths of disc for diffuse and stellar components.
$rdstar = \frac{rddiff}{zdstar}$	[10.0]		Ratio between radial and vertical scale length.
tgal	[1.0, 3.0, 5.0, 7.0, 9.0, 11.0, 13.0]	Gyr	Age of the galaxy.
		BULGES	
t_fin <sup>a</sup>		Gyr	
t_win (flag) <sup>a</sup>	[0, 1]		If this parameter is equal to 0, then $t_{win}=20$ , if it is equal to 1, then $t_{win}=t_{inf}$
nu_sch <sup>a</sup>	[2.0]		
tau_inf <sup>a</sup>	[0.1, 1.0]	Gyr	
f_win <sup>a</sup>	[1.8e-3]		
m_inf <sup>a</sup>	[1.0e4, 1.0e5, 1.0e6, 1.0e7, 1.0e8]	$M_\odot$	
	[1.0e9, 1.0e10, 1.0e11, 1.0e12]		
t_inf <sup>a</sup>	[0.9, 1.0, 3.0, 5.0]	Gyr	
mmolfraz <sup>b</sup>	[0.0, 0.5, 1.0]		
rcloud <sup>b</sup>	[16.0]	pc	
etastart <sup>b</sup>	[0.1]	Gyr	
idz <sup>b</sup>	1.0		
dsug <sup>b</sup>	0.4545		
igeo <sup>b</sup>	1		Flag that sets the geometry of the system. In this case the King profile was used: $\rho = \rho_0 [1 + (r/r_c)^2]^{-\gamma}$ .
rcstar, rcdiff <sup>b</sup>	[0.03, 0.1, 0.5, 1.0, 3.0, 5.0, 10.0]	kpc	Parameters of the King profile for stars and diffuse matter.
tgal <sup>b</sup>	[1.0, 3.0, 5.0, 7.0, 9.0, 11.0, 13.0]	Gyr	

## 4.2 Integral and differential number counts

The key prediction of any model of the extragalactic background is the integral and differential number counts.. For the BM model the equation used to derive number counts was described above. The main product of the P2017 model as well as both E1 and E2 models are the cones containing coordinates, magnification coefficients due to the lensing and fluxes of objects in the wavelengths of interest. Thus the calculation of number counts is trivial.

The number counts were calculated for the following wavelengths: 70, 110, 250, 350, 650, 1100, 2000 $\mu$ m. Such a choice was made because this study focuses on the prediction of the infrared background parameters for the Millimetron mission. In the Table 4 instruments that performed observations in this wavelengths are listed. Brief information on them in given in Table 2.

Let’s pay close attention to each number counts plot.

**70 $\mu$ m.** The following instruments have performed observations in this wavelength: Herschel (the PACS detector), Spitzer (the MIPS detector), IRAS (60  $\mu$ m), Akari (65  $\mu$ m). Millimetron will perform observations with the SACS detector, in the band 1 (50  $\mu$ m – 90  $\mu$ m). Integral number counts are shown on Fig. 6, upper left panel, differential source counts can be found on Fig. 8, upper left panel. Number counts of all the four models considered demonstrate fair agreement with each other and with observational data. It should be noted that on this wavelength the influence from AGN is significant and it is responsible for the shape of the curve on large fluxes.

**110 $\mu$ m.** On this wavelength the observations were carried out by Herschel space telescope with the PACS instrument (100  $\mu$ m). Millimetron will perform observations with the SACS instrument

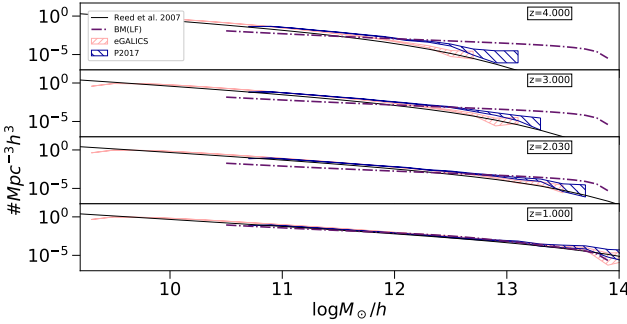


**Figure 4.** Mass functions from various models on different redshifts. From top to bottom:  $z = 4.0$ ,  $z = 3.0$ ,  $z = 2.030$ ,  $z = 1.0$ . The following mass functions are shown. 1) The mass function from Reed et al. (2007) that was used for taking into account the lensing effects in Béthermin et al. (2011). 2) BM: mass function derived from the luminosity function used in Béthermin et al. (2011) with the ratio 15. 3) The mass function of dark matter haloes from the eGALICS simulation (Cousin et al. (2015a), Cousin et al. (2015b)). 4) P2017.

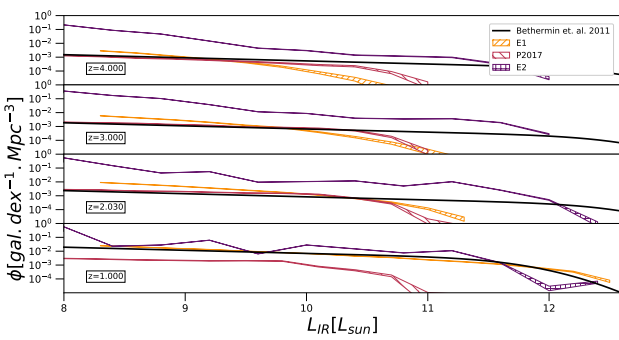


**Figure 5.** Luminosity functions of galaxies (without AGN contribution) of different models for four redshifts:  $z = 4.0$ ,  $z = 3.0$ ,  $z = 2.03$  and  $z = 1$ . 1) BM. 2) E1. 3) P2017. 4) E2.

**Table 4.** Left column: wavelength for which number counts were calculated. Second column: instruments which provided information about number counts in the wavelength considered. The wavelength in parentheses is present if the wavelength of observations differed from the wavelength in the left column. Right column – the corresponding detector of the Millimetron space observatory. Details see in text.

$\lambda, \mu\text{m}$	Instrument	Millimetron's detector
70	Herschel PACS (75 $\mu\text{m}$ ) Spitzer MIPS IRAS (60 $\mu\text{m}$ ) Akari (65 $\mu\text{m}$ )	SACS band 1
110	Herschel PACS IRAS (100 $\mu\text{m}$ )	SACS band 2
250	Herschel SPIRE	SACS band 3
350	Herschel SPIRE Apex SABOCA	SACS band 4 LACS band 4
650	–	LACS band 3
1100	Aztec camera	LACS band 2
2000	SPT	LACS band 1

in band 2 ( $90 \mu\text{m} - 160 \mu\text{m}$ ). Differential number counts are plotted on Fig. 8, upper right panel. Integral number counts are plotted on Fig. 6, upper right panel. All considered models correspond each other and observational data fairly well. On larger fluxes the tail of the E2 model is created by the AGN like at the  $70 \mu\text{m}$ .

**250μm.** On this wavelength the observations were performed by the Herschel space telescope with the SPIRE instrument and by the BLAST. Millimetron will perform observations with SACS in band 3 ( $160 \mu\text{m} - 300 \mu\text{m}$ ). Differential number counts are plotted on Fig. 8 on the lower left panel. Integral number counts are shown on Fig. 6, lower left panel. The E1 model shows drop off on fluxes larger than  $\sim 20\text{mJy}$  and predicts number counts only up to  $\sim 100\text{mJy}$ . The E2 model reproduces number counts up to  $\sim 500\text{mJy}$ . In contrast to shorter wavelengths AGN does not significantly contribute to the number counts. Such a trend remains for longer wavelengths. Slight deviation of the E2 model from observational data at fluxes  $\log_{10} S_{250\mu\text{m}} \sim 1.3^{+0.5}_{-0.5}$  should be noted.

**350μm.** On this wavelength observations were earlier performed by the Herschel space telescope with SPIRE instrument, by BLAST and PLANCK. Millimetron will perform observations with the SACS instrument in the band 4 ( $300 \mu\text{m} - 450 \mu\text{m}$ ). Differential number counts are plotted on Fig. 8 on lower right panel. Integral number counts are plotted on Fig. 6, lower right panel. The E1 model shows drop off on fluxes larger than  $\sim 10\text{mJy}$ . The E2 model does not demonstrate the drop off and predicts number counts up to higher fluxes  $\sim 300\text{mJy}$ . The slight deviation of the E2 model with observational data in the flux range  $6\text{mJy} < S_{350\mu\text{m}} < 30\text{mJy}$  should be noted.

**650μm.** On this wavelength the observations will be carried out by Millimetron with the LACS instrument in band 3 ( $450 \mu\text{m} - 850 \mu\text{m}$ ). Up to this day there is no information about the number counts in this wavelength. Differential number counts are plotted on Fig. 9, upper left panel. Integral number counts are plotted on Fig. 7, upper right panel. All the models considered demonstrate significant differences. But it is impossible to judge the correctness of the models due to the lack of observational data.

**850μm.** In this wavelength the observations were performed by PLANCK, SCUBA, LABOCA (870  $\mu\text{m}$ ), SCUBA-2, ALMA (870  $\mu\text{m}$ ). Millimetron will perform observations with the LACS instrument. The  $850 \mu\text{m}$  is the lower limit for the band 2 and the upper limit for band 3. Differential number counts are plotted on Fig. 9, upper right panel. Integral number counts are plotted on Fig. 7, upper right panel. The E1 and E2 models show fair agreement with each other up to the  $\sim 1\text{mJy}$  flux. The former shows significant drop off on larger fluxes. Some disagreement exists between all the models considered but it does not exceed the errors in the observational data.

**1100μm.** On this wavelength observations were performed by AzTEC and ALMA. Millimetron will perform observations with the LACS instrument in band 2 ( $850 \mu\text{m} - 1500 \mu\text{m}$ ). Differential number counts are plotted on Fig. 9, lower left panel. Integral number counts are shown on Fig. 7, lower left panel. The E1 and E2 models show fair agreement up to  $\sim 0.5\text{mJy}$ , but on larger fluxes the former shows a drop off. The differences between E2, P2017 and BM are noticeable but does not exceed observational errors.

**2000μm.** On this wavelength the observations were performed by PLANCK (2096  $\mu\text{m}$ ) and SPT. All the models considered show significant differences in predicted number counts but their validity can not be checked due to the lack of observational data for lower fluxes.

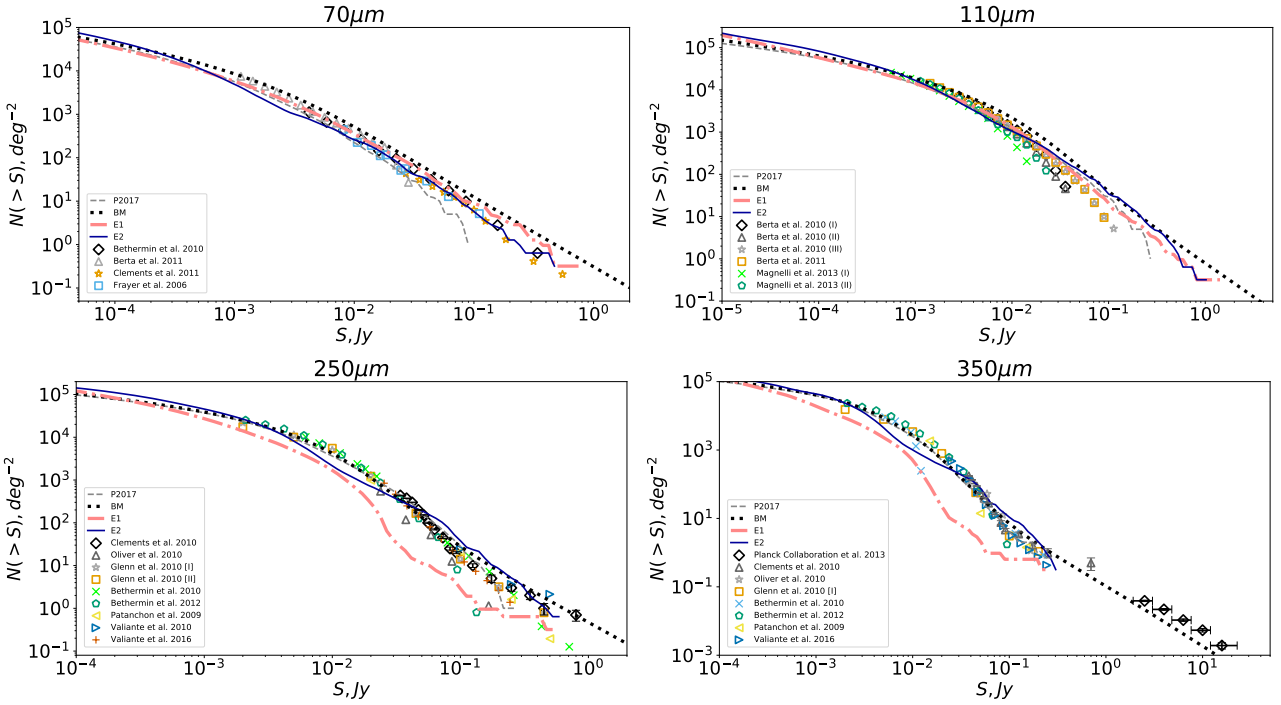


**Figure 6.** Integral source counts for different wavelengths. The predictions of four models are shown. 1) BM: number counts, calculated by the methods described in Béthermin et al. (2011). 2) P2017 model. 3) E1. 4) E2. The following observational data are shown: **70 $\mu\text{m}$**  Béthermin et al. (2010a) – Spitzer. Berta et al. (2011) – Herschel. Clements et al. (2011) – Spitzer. Frayer et al. (2006) – Spitzer. **110 $\mu\text{m}$**  Berta et al. (2010) – Herschel PEP GOODS-N field 100 $\mu\text{m}$ . Berta et al. (2010) – Herschel PEP LH field 100 $\mu\text{m}$ . Berta et al. (2010) – Herschel PEP COSMOS field 100 $\mu\text{m}$ . Berta et al. (2011) – Herschel PEP 100 $\mu\text{m}$ . Magnelli et al. (2013) – Herschel GOODS-S ultradeep field 100 $\mu\text{m}$ . Magnelli et al. (2013) – Herschel GOODS-N/S deep 100 $\mu\text{m}$ . **250 $\mu\text{m}$**  Clements et al. (2010) – Herschel. Oliver et al. (2010) – Herschel. Glenn et al. (2010)[I] – Herschel, multiply-broken power-law model. Glenn et al. (2010)[II] – Herschel, multiply-broken power-law model with the FIRAS prior. Béthermin et al. (2010b) – BLAST. Béthermin et al. (2012a) – Herschel. Patanchon et al. (2009) – BLAST. Valiante et al. (2010) – BLAST. Valiante et al. (2016) – Herschel. **350 $\mu\text{m}$**  Planck Collaboration et al. (2013) – PLANCK. Clements et al. (2010) – Herschel. Oliver et al. (2010) – Herschel. Glenn et al. (2010) – Herschel. Béthermin et al. (2010b) – BLAST. Béthermin et al. (2012a) – Herschel. Patanchon et al. (2009) – BLAST. Valiante et al. (2016) – Herschel.

### 4.3 Redshift distribution

It is a well known fact that on different wavelengths the dependence of contribution to the source counts from redshift varies significantly. Here we present 2d plots that show the dependence of contribution to number counts from objects with different fluxes on different redshifts. See Fig. 10, 11, 12, 13, 14, 15 and 16 respectively. These plots were created for all four models considered: BM, P2017, E1, E2. Let's pay close attention to each plot. The most important is the shape of the curve of dependence of contribution into source counts on redshift. In the text below we consider it's behaviours on different flux intervals.

**70 $\mu\text{m}$ .** The BM model due to it's semianalytic nature allows us to plot data on the whole  $S_\nu - z$  surface. For small fluxes  $\log_{10}(S_\nu) \sim -2$  the contribution to source counts is uniform on the whole range of redshifts with a smooth peak near  $z \sim 1$ . Towards the larger fluxes there is a tendency of increasing the contribution from sources at  $z \leq 1$  and the peak itself moves towards lower redshifts. At  $\log_{10}(S_\nu) = 1$  the greatest contribution is from objects at  $0 < z < 1$ . For even larger fluxes there is a trend of increasing the contribution from galaxies at lower redshift.

The situation for the P2017 model is quite different. At low fluxes  $\log_{10}(S_\nu) < -2$  the contribution to the number counts is uniform on all redshifts with gradual decline towards higher redshifts. If we go to higher fluxes the shape of the dependence on redshift

does not change but on certain redshift a drop off appears. It shifts towards lower redshifts with the increase of the flux.

For the E1 model the picture is as follows. At fluxes in the interval  $-2 < \log_{10}(S_\nu) < 0$  the curve is quite uniform with noticeable growth near  $z = 0$ . There is also a drop off at  $z = 2$ . It's presence can be explained by the form of the equation used to derive luminosity from the halo mass. It's parameters change at this redshift (see equation 15). At fluxes larger than 0.5 the shape of the dependence does not change significantly but the drop off moves towards  $z = 0$ .

The prediction of the E2 model has the following properties. The feature at  $z = 2$  is not present. For all fluxes the dependence on redshift is uniform with noticeable decrease on low redshifts. At large fluxes  $\log_{10}(S_\nu) \geq 2.0$  the main contribution is from active galactic nuclei at low redshifts.

**110 $\mu\text{m}$ .** For the BM model the situation does not differ from 70 $\mu\text{m}$ . But for large fluxes  $3 \leq \log_{10}(S_\nu) < 4$  the contribution of sources up to  $z = 1-2$  becomes uniform and for larger redshifts a gradual decline can be observed.

For the P2017 model the shape of the 2d plot does not show any significant differences from 70 $\mu\text{m}$ .

The same is true for the E1 and E2 models.

**250 $\mu\text{m}$ .** The shape of the 2d plot for this wavelength for the BM model changes significantly. On low fluxes  $-2 \leq \log_{10}(S_\nu) \leq -1$  there is a peak at  $z = 1$ , a decline at  $z = 1-2$  and a further gradual decrease towards higher redshifts. On fluxes  $\log_{10}(S_\nu) \approx 0$  the peak

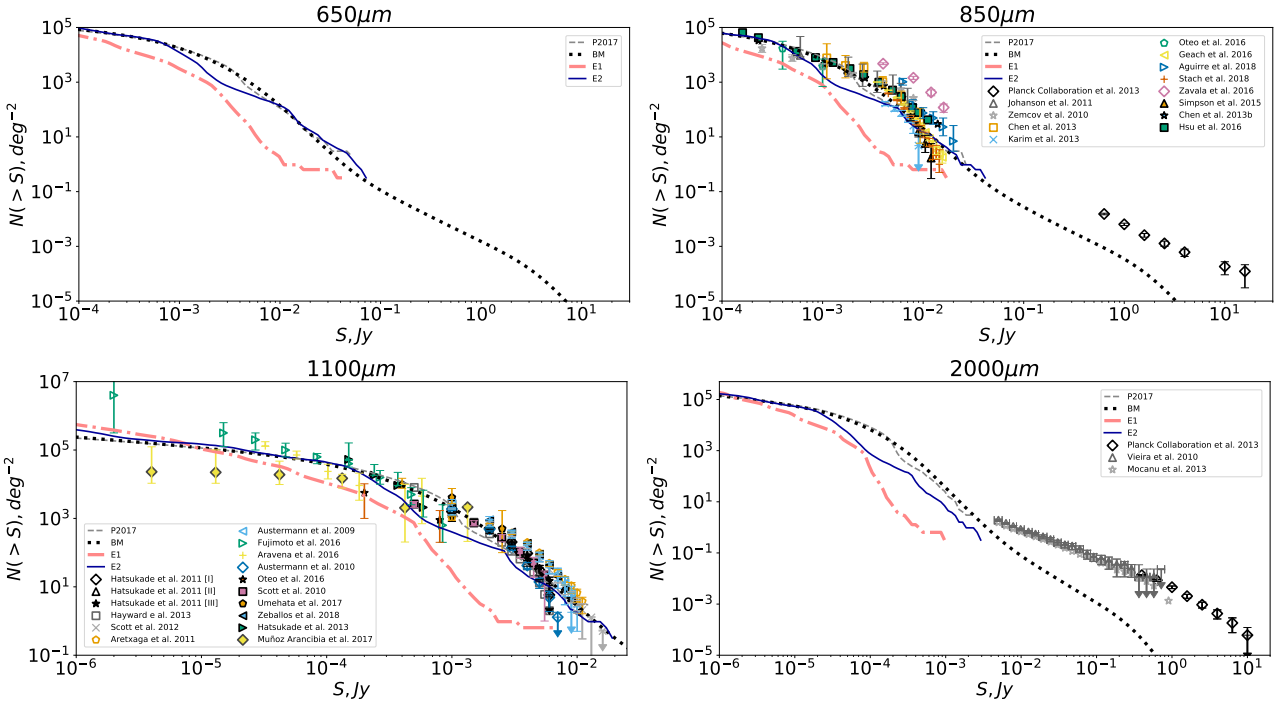


**Figure 7.** Integral source counts for four different wavelengths. 1) BM: counts calculated by the approach described in Béthermin et al. (2011). 2) The P2017 model. 3) E1. 4) E2. The following observational data are shown: **850 $\mu$ m** Planck Collaboration et al. (2013) – PLANCK. Johansson et al. (2011) – LABOCA(APEX) 870 $\mu$ m. Zemcov et al. (2010) – SCUBA. Chen et al. (2013a) – SCUBA-2. Karim et al. (2013) – ALMA 870 $\mu$ m. Oteo et al. (2016) – ALMA 870 $\mu$ m. Geach et al. (2017) – SCUBA-2. Aguirre et al. (2018) – LABOCA/ACT 870 $\mu$ m. Stach et al. (2018) – ALMA 870 $\mu$ m. Zavala et al. (2017) – SCUBA 2. Simpson et al. (2015) – SCUBA 2. Chen et al. (2013b) – SCUBA 2. Hsu et al. (2016) – SCUBA 2. **1100 $\mu$ m** Hatsukade et al. (2011) – AzTEC/ASTE ADFS field. Hatsukade et al. (2011) – AzTEC/ASTE SXDF field. Hatsukade et al. (2011) – AzTEC/ASTE SSA22 field. Hayward et al. (2013) – model predictions. Scott et al. (2012) – AzTEC. Aretxaga et al. (2011) – AzTEC. Austermann et al. (2009) – AzTEC. Fujimoto et al. (2016) – ALMA 1.2 mm. Aravena et al. (2016) – ALMA 1.2 mm. Austermann et al. (2010) – AzTEC. Oteo et al. (2016) – ALMA 1.2 mm. Scott et al. (2010) – AzTEC. Umehata et al. (2017) – ALMA 1.1 mm. Zeballos et al. (2018) – AzTEC 1.1 mm. Hatsukade et al. (2013) – ALMA 1.3 mm. Muñoz Arancibia et al. (2017) – ALMA 1.1 mm. **2000 $\mu$ m** Planck Collaboration et al. (2013) – Planck 143GHz(2096  $\mu$ m). Vieira et al. (2010) – SPT. Mocanu et al. (2013) – SPT.

starts to widen and shift towards higher  $z$ . At  $\log_{10}(S_\nu) \simeq 2$  two peaks appear, one at low redshifts and another at  $z = 2$ . Towards even larger fluxes the contribution from the second peak decreases and the contribution from the nearby galaxies increases rapidly.

As for the P2017 model the shape of the dependence on redshift has almost identical shape at all fluxes. Gradual increase towards  $z \sim 1.5$  then gradual decline towards higher redshifts. Starting from  $\log_{10}(S_\nu) \sim -1$  a drop off appears on high  $z$  that shifts towards lower redshifts with the increase of the flux.

The behaviour of the prediction for the E1 model is as follows. On small fluxes  $\log_{10}(S_\nu) \sim -2$  there is an increase towards  $z = 1$ , a plateau up to  $z = 2$  then a gradual decline. At higher luminosities the shape of the dependence does not change for redshifts lower than  $z = 2$ . At higher redshifts a drop off is present and it shifts towards low redshift with the increase of the flux. In the flux interval  $0 \geq \log_{10}(S_\nu) \geq 1$  the shape of the curve and the position of the drop off at  $z = 2$  does not depend on the flux.

The shape of the curves of the E2 model is similar for all fluxes  $\log_{10}(S_\nu) > -2$ . Initial increase, plateau and a gradual decrease towards higher redshifts. At fluxes  $\log_{10}(S_\nu) > -2$  a drop off at higher redshifts is present which shifts towards lower redshifts with the increase of the flux. The point is that on intermediate fluxes the main contribution comes from high redshift objects. It should be mentioned that the AGN contribution is still present on high fluxes and low redshifts but is much lower than it is at shorter wavelengths. Towards higher  $\lambda$  this trend will persist.

**350 $\mu$ m.** For all four models considered the shape of the 2d planes does not differ significantly from 250  $\mu$ m.

**650 $\mu$ m.** On this wavelength the shape of the 2d distribution changes significantly.

The BM model shows a peak near  $z = 1$  on small fluxes  $\log_{10}(S_\nu) \simeq -2$ . The decrease is quite steep towards low redshift and smooth towards higher  $z$ . At higher fluxes this peak becomes more prominent especially at  $\log_{10}(S_\nu) \simeq 0$ . At highest fluxes there are two peaks – on small redshifts and in the vicinity of  $z = 2$ .

In the P2017 model the dependence of the contribution to the number counts from redshift does not depend on flux for all the range of  $S_\nu$ . The gradual rise and decline is observed. In other words it can be said that in number counts on 650  $\mu$ m contribute objects from all the redshift range.

The E1 model on small fluxes  $-4 \leq \log_{10}(S_\nu) \leq -2$  shows gradual increase up to  $z = 2$  and decrease towards higher redshifts. On higher fluxes the general shape does not change but the cut off on high redshift moves towards  $z = 2$ . The area around  $\log_{10}(S_\nu) \sim 0.5$  is quite curious. There are no objects with redshifts greater than  $z > 2$ . At fluxes  $\log_{10}(S_\nu) > 0.5$  the main and only contributors to the number counts are the objects with redshifts  $1.5 < z < 2$  and the local ones.

The shape of the curve of the E2 model is similar in wide range of fluxes  $\log_{10}(S_\nu) < 0$ . It shows gradual rise towards  $z \sim 0.5$ , then plateau up to  $z \sim 4.5$ . On high fluxes  $\log_{10}(S_\nu) > 0.5$  two separate peaks can be clearly seen. In other words on intermediate and low

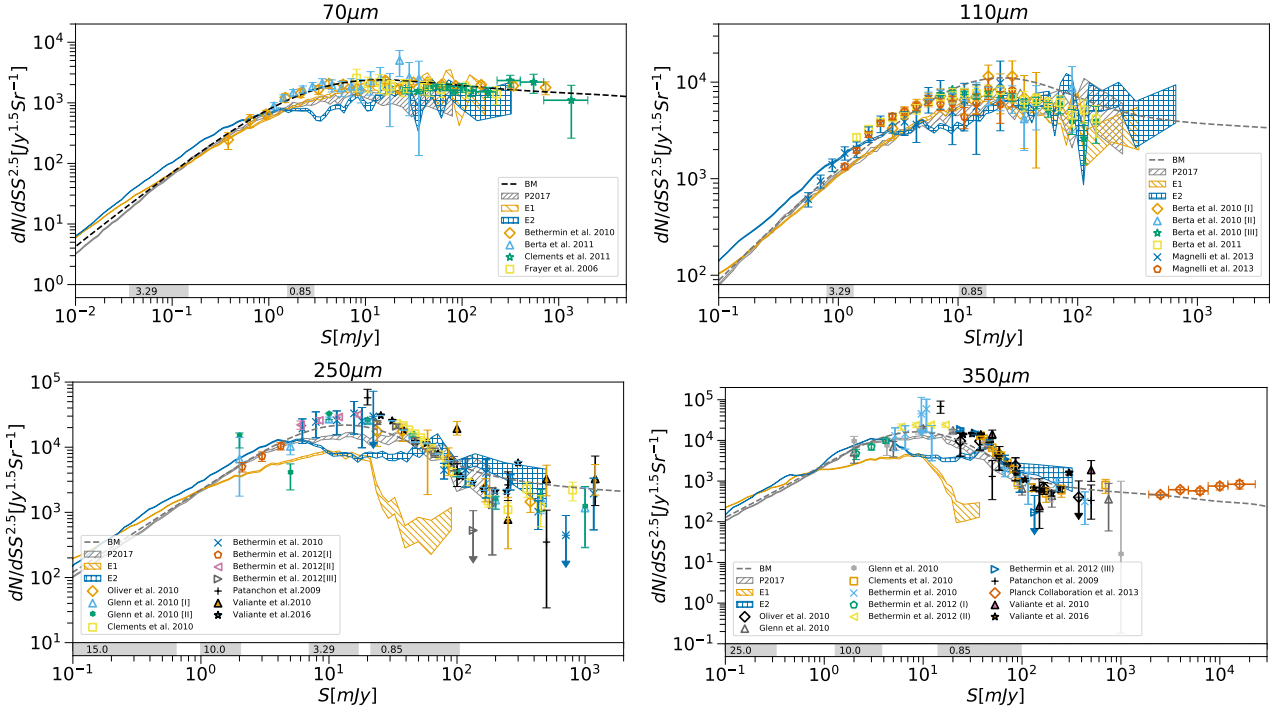


**Figure 8.** Differential source number counts. Common for all plots: 1) Predictions of the BM model. 2) The P2017 model. 3) E1. 4) E2. Various markers show data from the following papers: **70μm** Béthermin et al. (2010a) – Spitzer. Berta et al. (2011) – Herschel. Clements et al. (2011) – Spitzer. Frayer et al. (2006) – Spitzer. **110μm** Berta et al. (2010) – Herschel/PEP GOODS-N 100 μm. Berta et al. (2010) – Herschel/PEP LH 100 μm. Berta et al. (2010) – Herschel/PEP COSMOS 100 μm. Berta et al. (2011) – Herschel/PEP 100 μm, all fields. Magnelli et al. (2013) – Herschel/PACS GOODS-S 100 μm. Magnelli et al. (2013) – Herschel/PACS GOODS-N/S 100 μm. **250μm** Oliver et al. (2010) – Herschel Multi-tiered Extra-galactic survey(HerMES): SPIRE. Glenn et al. (2010) [I] – Herschel: differential number counts constraints for a multiply-broken power-law model. Glenn et al. (2010) [II] – Herschel: differential number counts constraints for a multiply-broken power-law model with the FIRAS prior. Details see in the paper. Clements et al. (2010) – Herschel. Béthermin et al. (2010b) – BLAST. Béthermin et al. (2012a) [I] – Herschel, Stacking (GOODS-N). Béthermin et al. (2012a) [II] – Herschel, Stacking (COSMOS). Béthermin et al. (2012a) [III] – Herschel, Resolved (COSMOS). Patanchon et al. (2009) – BLAST. Valiante et al. (2010) – BLAST. Valiante et al. (2016) – Herschel. **350μm** Legend is the same as for 250 μm, with one exception: Planck Collaboration et al. (2013) – PLANCK. Lower panels – intervals of the confusion noise estimations for different sizes of the main mirror. Details see in text.

fluxes objects from all redshifts contribute to the number counts, mainly from  $0.5 < z < 4.5$ .

**1100μm.** The BM model shows the following behaviour. On small fluxes  $\log_{10}(S_\nu) \approx -2$  a slight peak is present at  $z = 1$ . Towards larger fluxes  $-1 < \log_{10}(S_\nu) \approx -0.5$  the peak widens and moves towards larger redshifts. From the flux  $\log_{10}(S_\nu) \approx 0.5$  and higher the curve takes the following bimodal shape. Close objects give significant contribution. There is a significant depression at  $z \sim 0.5$  followed by gradual rise and from  $z \sim 2$  the curve becomes uniform and shows no further dependence on redshift.

As for the model of P2017 the shape of the 2d distribution does not qualitatively differ from the one for  $\lambda = 650\mu\text{m}$ .

The same is true for the E1 and E2 models. The whole 2d surface is shifted towards larger fluxes.

**2000μm.** As for the BM model, on the small fluxes  $\log_{10}(S_\nu) = -2$  the contribution is uniform on all redshift with exception of a prominent peak around  $z \approx 1$ . When the flux is about  $\log_{10}(S_\nu) \approx -1$  the behaviour is as follows. The contribution increases from  $z = 0$  towards  $z \approx 1$  while on larger redshifts it stays almost constant.

On larger fluxes two peaks become apparent. The first one is at low  $z$  and shifts towards  $z = 0$  with the increase of the flux. The second one on larger redshifts becomes less and less prominent with the increase of the flux.

As for the P2017, the shape of the curve does not depend on

the flux. The gradual increase towards  $z = 2$  and decrease to even higher redshifts is observed.

The E1 model predicts number counts only up to fluxes  $3 \times 10^{-1} \text{ mJy}$ . For sources with flux  $\log_{10}(S_{2000\mu\text{m}}) > -2$  the upper limit of sources is on  $z = 2$ . With the increase of redshift the contribution into source counts also increases.

In the E2 model on fluxes lower than  $\log_{10}(S_\nu) = -2$  there is a rise up to  $z \approx 1$ , a plateau up to  $z = \approx 4.5$  and a decrease towards even higher redshifts. On larger fluxes two disconnected regions are present, at low redshifts and at  $z = 1-1.5$ .

All the above said leads to the following short takeaway. There is an obvious tendency of increasing of the contribution of distant galaxies on lower fluxes and longer wavelngts. The changes in the redshift distribution of sources between adjacent wavelength bands are the most prominent for the pairs of 110–250 microns, 350–650 and 1100–2000 microns. There are significant differences between four models we consider. BM and E2 models show a presence of two peaks in the redshift distribution of source counts for relatively high fluxes, while P17 and E1 do not show this feature. All models show a very different behaviour at high redshifts,  $z > 4.5$ . P2017 and E1 models show a significant dropoff at some redshift which changes with flux. These differences show that the analysis of the distribution of sources on the redshift–flux plane in observations and models can be a challenging test of these models.

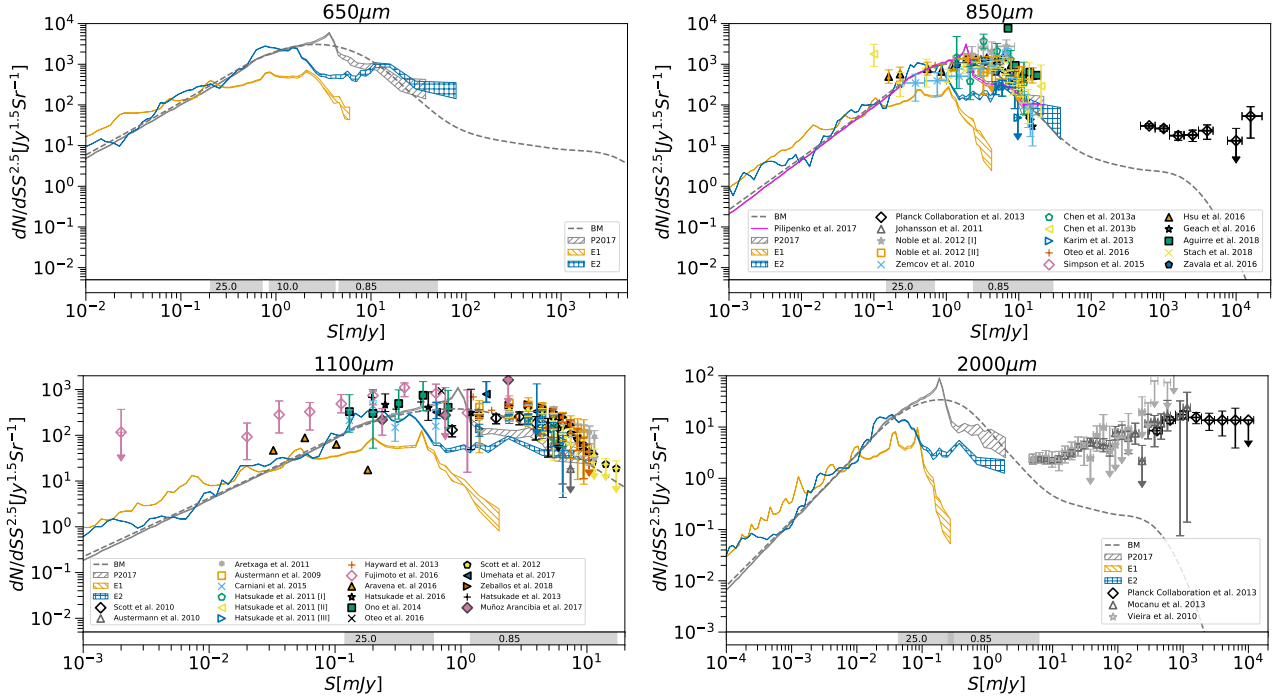


**Figure 9.** Differential source number counts. Common for all plots: 1) Predictions of the BM model. 2) The P2017 model. 3) E1, 4) E2. Various markers show data from the following papers: **850 $\mu$ m** Planck Collaboration et al. (2013) – PLANCK. Johansson et al. (2011) – APEX LABOCA 870 $\mu$ m. Noble et al. (2012) – SCUBA, lensed sample. Noble et al. (2012) – SCUBA, control sample. Zemcov et al. (2010) – SCUBA. Chen et al. (2013a) – SCUBA-2. Chen et al. (2013b) – SCUBA-2. Karim et al. (2013) – ALMA 870  $\mu$ m. Oteo et al. (2016) – ALMA 870  $\mu$ m. Simpson et al. (2015) – ALMA 870  $\mu$ m. Hsu et al. (2016) – SCUBA-2. Geach et al. (2017) – SCUBA-2. Aguirre et al. (2018) – LABOCA/ACT 870  $\mu$ m. Stach et al. (2018) – ALMA 870  $\mu$ m. Stach et al. (2018) – SCUBA-2. **1100 $\mu$ m** Scott et al. (2012) – AzTEC GOODS-S field. Scott et al. (2012) – AzTEC. Austermann et al. (2010) – AzTEC. Aretxaga et al. (2011) – AzTEC COSMOS field. Austermann et al. (2009) – AzTEC COSMOS field. Carniani et al. (2015) – ALMA. Hatsukade et al. (2011) – Aztec ADF-S field. Hatsukade et al. (2011) – Aztec SXDF field. Hatsukade et al. (2011) – Aztec SSA22 field. Hayward et al. (2013) – model predictions. Fujimoto et al. (2016) – ALMA 1.2 mm. Aravena et al. (2016) – ALMA 1.2 mm. Hatsukade et al. (2016) – AzTEC/ASTE. Ono et al. (2014) – ALMA 1.2 mm. Oteo et al. (2016) – ALMA 1.2 mm. Umehata et al. (2017) – ALMA. Zeballos et al. (2018) – Aztec. Hatsukade et al. (2013) – ALMA 1.3 mm. Muñoz Arancibia et al. (2017) – ALMA 1.1 mm. **2000 $\mu$ m** Planck Collaboration et al. (2013) – PLANCK 143GHz (2096  $\mu$ m). Mocanu et al. (2013) – SPT-SZ survey. Vieira et al. (2010) – SPT. Lower panels – range of the confusion noise estimates for different diameters of the main mirror. Details see in text.

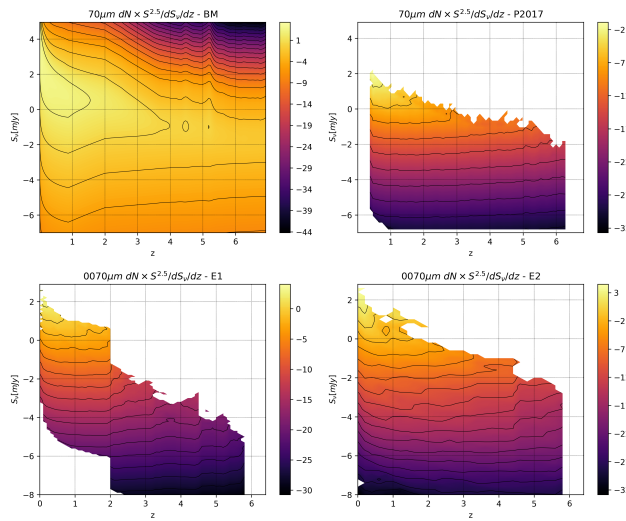


**Figure 10.** Contribution into differential number counts  $dN/dSS^{2.5}$  from sources with different fluxes  $S_\nu$  on different redshifts. Wavelength  $\lambda = 70\mu\text{m}$ . Upper left panel – BM. Upper right panel – P2017. Lower left panel – E1. Lower right panel – E2.

#### 4.4 Extragalactic Background Light

In this section we consider the dependence of the Extragalactic Background Light on the wavelength  $\lambda$  (SED). We also plot the contribution to it from objects with different luminosities and from objects in different redshift intervals.

The Extragalactic Background Light SED for four cuts in redshift is shown on Fig. 17. All four models are plotted. Let us consider these redshift intervals individually.

**0.0 <  $z$  < 1.0.** The EBL SED is shown on Fig. 17, upper left panel. All models show fair agreement with each other. The BM model demonstrates slight disagreement with observational data from Viero et al. (2013). The dashed line shows the E2 EBL SED without the contribution from AGN. As was already mentioned before, the contribution from AGN is significant only for relatively short wavelength  $\lambda \leq 100\mu\text{m}$ .

**1.0 <  $z$  < 2.0.** The EBL SED is shown on Fig. 17, upper right panel. All models show fair agreement with each other and with observational data. It should be noted that the contribution of AGN is significant here on short wavelengths  $\lambda < 100\mu\text{m}$ .

**2.0 <  $z$  < 3.0.** The EBL SED is plotted on Fig. 17, lower left panel. On this redshift interval three of the four models agree with each other. The outstanding one is E1. That is due to the utilized  $M - L$  ratio which parameters change at  $z = 2$ . It should be noted that the contribution of AGN is less prominent.

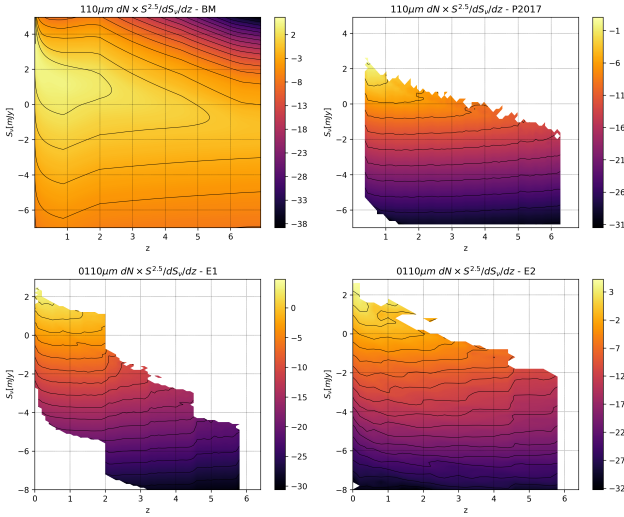


**Figure 11.** Contribution into differential number counts  $dN/dSS^{2.5}$  from sources with different fluxes  $S_\nu$  on different redshifts. Wavelength  $\lambda = 110\mu\text{m}$ . The legend is equal to the one of Fig. 10.

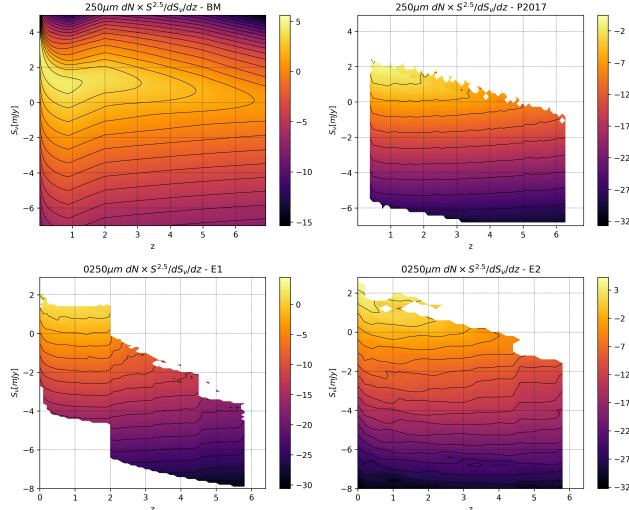


**Figure 12.** Contribution into differential number counts  $dN/dSS^{2.5}$  from sources with different fluxes  $S_\nu$  on different redshifts. Wavelength  $\lambda = 250\mu\text{m}$ . The legend is equal to the one of Fig. 10.

$z > 3.0$ . The EBL SED is plotted on the Fig. 17, lower right panel. In this redshift range the best agreement is demonstrated by the BM model and E2. The E1 model has a couple of orders of magnitude difference due to the reasons described above. The important fact is that the contribution from AGN is insignificant. It is worth noting that observational data from Viero et al. (2013) lie significantly higher than all four curves.

On this plot the total EBL sed is also shown. All models show good agreement with each other. It should be noted that the differences between total EBL spectra of the four models considered is lower than the discrepancy between observational data from various papers.

The EBL SED for four luminosity cuts is shown on Fig. 18. Let us pay close attention to each plot.

$L < 10^6 L_\odot$ . The EBL SED is plotted on Fig. 18, upper left panel. In this luminosity bin BM and E1 show good agreement with

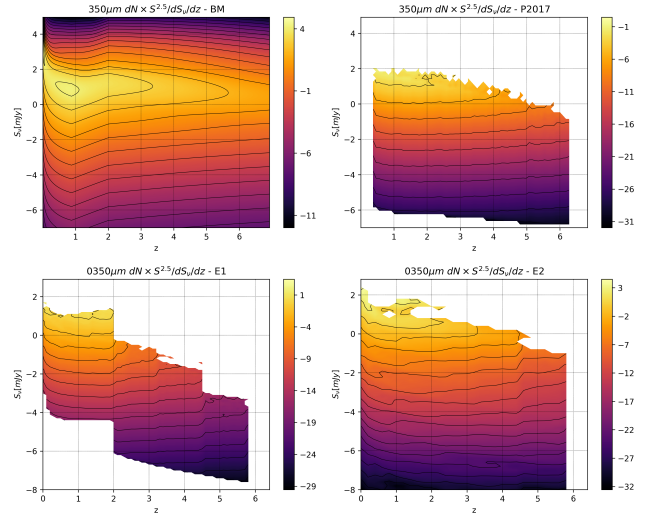


**Figure 13.** Contribution into differential number counts  $dN/dSS^{2.5}$  from sources with different fluxes  $S_\nu$  on different redshifts. Wavelength  $\lambda = 350\mu\text{m}$ . The legend is equal to the one of Fig. 10.

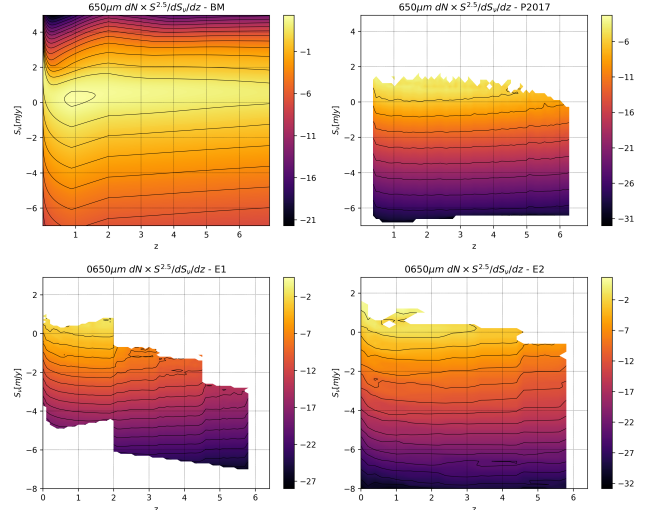


**Figure 14.** Contribution into differential number counts  $dN/dSS^{2.5}$  from sources with different fluxes  $S_\nu$  on different redshifts. Wavelength  $\lambda = 650\mu\text{m}$ . The legend is equal to the one of Fig. 10.

each other. The E2 and P2017 show severe discrepancy. The contribution into the EBL from AGN in this luminosity range is small. On this plot the total EBL SED is also shown. As was discussed above, the total EBL SEDs predicted by different models agree fairly well. It can be seen that the contribution to EBL from galaxies with such low luminosities is of order  $\sim 10^{-4}$ .

$10^6 L_\odot < L < 10^8 L_\odot$ . The EBL SED is plotted on Fig. 18, upper right panel. In this luminosity range all four models predict different shapes of the EBL SED. The contribution from AGN is very small.

$10^8 L_\odot < L < 10^{10} L_\odot$ . The EBL SED is shown on Fig. 18, lower left panel. All models show some degree of agreement with each other. On the short wavelengths  $\lambda < 100\mu\text{m}$  the contribution of AGN starts to show itself.

$10^{10} L_\odot < L < 10^{12} L_\odot$ . The EBL SED is plotted on the Fig. 18, lower right panel. In this wavelength range the models

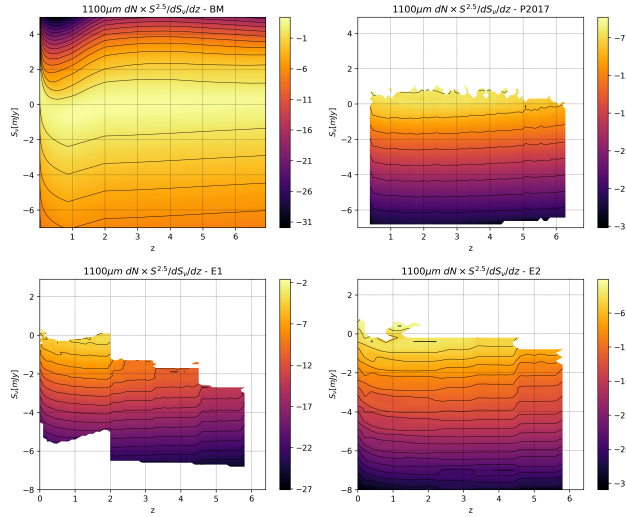


**Figure 15.** Contribution into differential number counts  $dN/dSS^{2.5}$  from sources with different fluxes  $S_v$  on different redshifts. Wavelength  $\lambda = 1100\mu\text{m}$ . The legend is equal to the one of Fig. 10.

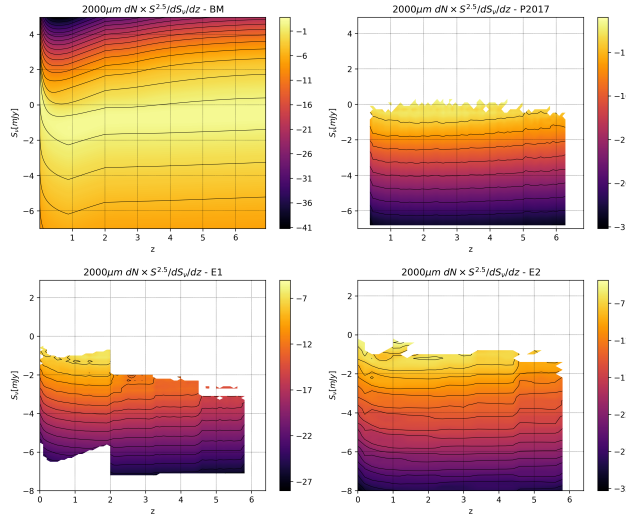


**Figure 16.** Contribution into differential number counts  $dN/dSS^{2.5}$  from sources with different fluxes  $S_v$  on different redshifts. Wavelength  $\lambda = 2000\mu\text{m}$ . The legend is equal to the one of Fig. 10.

show fair agreement with each other. The BM model shows different behavior at the shortest wavelengths, while the E1 model on wavelengths larger than  $100\mu\text{m}$ .

#### 4.5 The confusion noise

Three criteria of the confusion noise estimation were used in this paper.

This first criterion can be defined as the minimal completeness of detection of sources with flux greater than  $S_{lim}$ . It is defined through a fraction of sources that are lost in the detection process when a neighbor with a flux greater than  $S_{lim}$  is at an angular distance that makes the separation impossible.

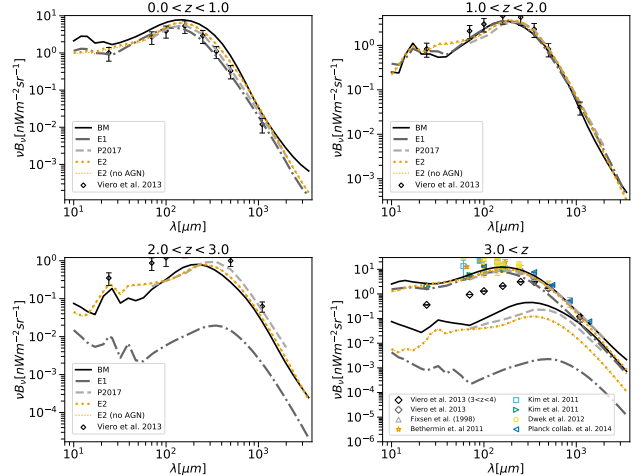


**Figure 17.** Extragalactic background light spectrum. Legend is the same for all four subplots. 1) The predictions of the BM model. 2) E1. 3) P2017. 4) E2. The four plots shown demonstrate four redshift slices. Upper left panel:  $0.0 < z < 1.0$ . Upper right panel:  $1.0 < z < 2.0$ . Lower left panel:  $2.0 < z < 3.0$ . Lower right panel:  $3.0 < z$ . Upper group of curves are the EBL SEDs for the whole redshift range. The following observational data are shown on the plot. Upper panels and lower left one: Viero et al. (2013). Lower right panel: 1) Viero et al. (2013) ( $3.0 < z < 4.0$ ). 2) Viero et al. (2013). 3) Fixsen et al. (1998). 4) Compiled observational data from Béthermin & Dole (2011). Detail and links to actual publications see in the paper. 5) Kim et al. (2012), Akari. 6) Kim et al. (2012), Spitzer. 7) Compiled observational data from Dwek & Krennrich (2013). Links to the actual publications see in the paper. 8) Planck Collaboration et al. (2014).

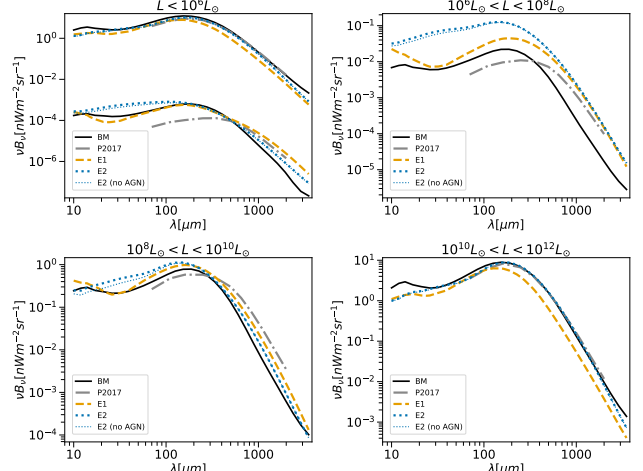


**Figure 18.** Contributions from galaxies with different luminosities to the EBL. Legend is the same for all four plot and is analogous to the one of Fig. 17. Upper left panel:  $L < 10^6 L_\odot$ . Upper right panel:  $10^6 L_\odot < L < 10^8 L_\odot$ . Lower left panel:  $10^8 L_\odot < L < 10^{10} L_\odot$ . Lower right panel:  $10^{10} L_\odot < L < 10^{12} L_\odot$ .

Frequently the following formula is used (Dole et al. 2003):

$$N_{SDC} = - \frac{\log(1 - P(< \theta_{min}))}{\pi k^2 \theta_{FW}^2} \quad (20)$$

Here the probability  $P = 0.1$  and  $k = 0.8$ , while  $\theta_{FW}$  is a full width at half magnitude of the beam profile.

The second criterion is called photometric and is calculated in

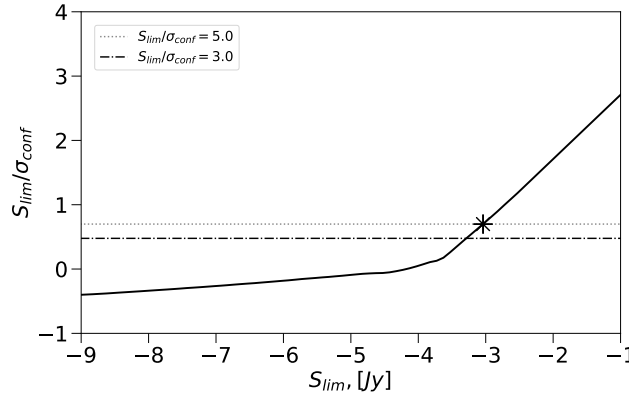


**Figure 19.** The signal to noise ratio vs the confusion limit for the 10.0-m telescope and  $\lambda = 2000\mu\text{m}$ . Horizontal lines show  $S_{lim}/\sigma_{conf} = 5$  (dashed line) and  $S_{lim}/\sigma_{conf} = 3$  (dot-dashed line). For this plot number counts from the P2017 model were used.

the following way (Dole et al. 2003). First, the response amplitude  $x$  from the source with flux  $S$  and coordinates  $\theta, \phi$  is defined:

$$x = Sf(\theta, \phi) \quad (21)$$

Where  $f(\theta, \phi)$  is the two-dimensional shape of the beam profile. The average number of responses  $R(x)$  with amplitudes from  $x$  to  $x + dx$  from sources in the element of the beam profile  $d\Omega$  with coordinates  $(\theta, \phi)$ , where  $d\Omega = 2\pi\theta d\theta d\phi$  can be found in the following way:

$$R(x)dx = \int_{\Omega} \frac{dN}{dS} dS d\Omega \quad (22)$$

The dispersion of the measurement in the beam due to the extragalactic sources with flux lower than  $S_{lim}$  is expressed as:

$$\sigma_c^2 = \int_0^{x_{lim}} x^2 R(x)dx \quad (23)$$

where  $x_{lim} = S_{lim}f(\theta, \phi)$  is the upper limit of response on large fluxes. Dole et al. (2003) rewrite this in the following way

$$\sigma_c^2 = \int f^2(\theta, \phi) d\theta d\phi = \int_0^{S_{lim}} S^2 \frac{dN}{dS} dS \quad (24)$$

Here  $dN/dS$  is the differential number counts expressed in  $\text{Jy}^{-1}\text{sr}^{-1}$ ,  $\sigma_c$  is the confusion noise,  $S_{lim}$  the confusion limit. As a next step the photometric criterion  $q$  must be set. The common choice is 3 or 5. Then the following equation must be solved.

$$q = \frac{S_{lim}}{\sigma_{cpho}(S_{lim})} \quad (25)$$

The Fig. 19 illustrates the search for solution for  $d = 10.0$  m and the wavelength  $\lambda = 2000\mu\text{m}$ .

The third criterion is called ‘Probability of Deflection’ –  $P(D)$ . It is calculated in the following way (see, e.g. (Glenn et al. 2010)). The average density of sources per solid angle with flux in the interval from  $x$  to  $x + dx$ .

$$R(x)dx = \int_{\Omega} \frac{dN}{dS} \left( \frac{x}{b} \right) b^{-1} d\Omega dx \quad (26)$$

The probability distribution function for a single pixel is:

$$P(D) = F_{\omega}^{-1} \left[ \exp \left( \int_0^{\infty} R(x) \exp(i\omega x) dx - \int_0^{\infty} R(x) dx \right) \right] \quad (27)$$

where  $F_{\omega}^{-1}$  is the inverse Fourier transform.

Different parameters can be used in order to quantify the confusion limit. The authors of Béthermin et al. (2011) have used, for example, an interquartile. The Figs. 20–24 show the confusion noise vs wavelength for the following values of the main mirror diameter: 0.85 m, 3.29 m, 10.0 m, 15.0 m, 25.0 m.

As long as we consider only space missions we suppose the diffraction quality of the imaging. In this case the confusion noise depends only on angular resolution of the telescope and the shape of the source number counts curve. The resolution of the instrument depends on the diameter of the main mirror and the wavelength. Thus the general trend of increasing of the confusion noise with increase of  $\lambda$  and decrease of diameter is superimposed on the effects caused by the change in the shape of the number counts curves. This is how the plotted shapes of the dependencies of confusion noise on wavelength can be explained.

It is quite curious that for every diameter of the main mirror the curves have peak on a certain wavelength and a decline towards lower and higher wavelengths.

It is worth considering which part of the number counts curve influences the confusion noise estimates. Let’s again pay attention to the Figs. 8 and 9. Each has a lower panel where the intervals of confusion noise estimates are plotted. They are defined as  $\sigma_{min} = \min(\sigma_{SDC}, \sigma_{P(D)})$  and  $\sigma_{max} = \max(\sigma_{SDC}, \sigma_{P(D)})$ . Numbers correspond to the diameter of the mirror. On the plots for  $70\mu\text{m}$ ,  $110\mu\text{m}$ ,  $250\mu\text{m}$ ,  $350\mu\text{m}$  the confusion noise estimation intervals for large diameters are not plotted because the confusion noise is lower than the minimal value on the X axis. On some plots intermediate diameters are not shown because the corresponding intervals overlap thus making the plot uninformative. With the help of these plots the two following conclusions can be made.

At first let us find out whether the confusion noise estimations lie within the flux ranges for which we have observational data. For the  $d = 0.85$  m this holds true for all the wavelength range. This is pretty obvious because after Spitzer there were plenty of other space telescopes. For  $3.29$  m observational data exists for all wavelengths longer than  $70\mu\text{m}$ . For  $10$  m (Millimetron) this is true for  $250$ – $1100\mu\text{m}$ , but not for  $2000\mu\text{m}$ . At  $2000\mu\text{m}$  we have number counts estimates only for large fluxes. For diameters  $15$ – $25$  m we have number counts for  $850\mu\text{m}$  and  $1100\mu\text{m}$  but not for  $2000\mu\text{m}$ .

As can be seen from the number counts plots all models considered show good agreement on low fluxes and some level of discrepancy on bright fluxes. This is especially the case for the E1 model that shows a drop for some wavelengths. Let us find for which mirror diameters and wavelengths the estimations of the confusion noise lie in the interval where the differences between the models start to play a significant role. This question can be formulated another way. ‘For which diameters and wavelengths in order to estimate the confusion noise it is possible to use the simplest model (like P2017 or E1) the only ingredients of which are the halo mass function, the  $M_{halo}$ – $L$  ratio and the SED library of local galaxies.’ The answer is as follows.

$70\mu\text{m}$  and  $110\mu\text{m}$ ) The answer is positive for all the diameters considered.

$250\mu\text{m}$ ) The simple approach is not valid for  $d = 0.85$  m.

$350\mu\text{m}$ ) The simple approach is not valid for  $0.85$  m and  $3.29$  m.

$650\mu\text{m}$ ) The simple approach is valid only for  $15$  m and  $25$  m.

$850\mu\text{m}$ ) The simple approach is valid only for  $25$  m.

$1100\mu\text{m}$  and  $2000\mu\text{m}$ ) More complex algorithms must be used.

This trend is quite obvious but is definitely worth noting because it bears great implications.

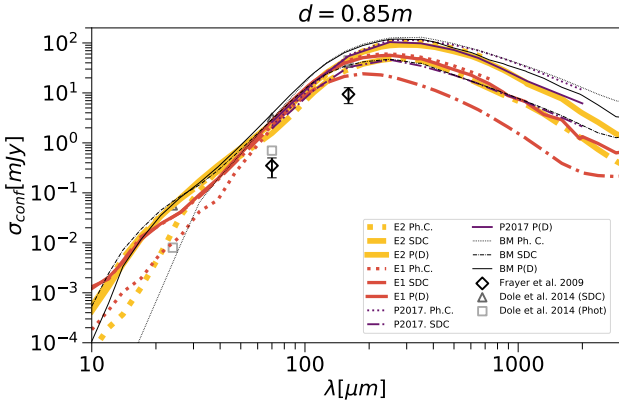


**Figure 20.** Diameter of the main mirror 0.85 m. The confusion noise vs wavelength for four models considered and three estimation methods. That gives total 12 curves. First group – BM. Second group – the P2017 model. Third group – E1 model. Fourth group – E2. Dotted lines – photometric criterion. Dot-dashed lines – SDC (Source density criterion). Solid lines – P(D) criterion. Estimations from the following papers are also plotted: 1) Frayer et al. (2009). 2) Dole et al. (2004) (SDC). 3) Dole et al. (2004) (Photometric criterion).

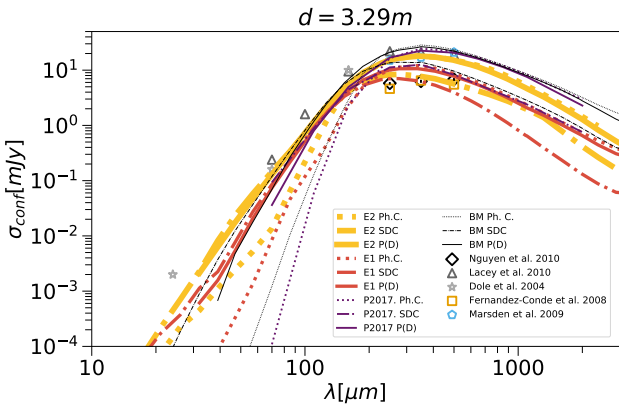


**Figure 21.** Diameter of the main mirror 3.29 m. The confusion noise vs wavelength for four models considered and three estimation methods. The legend is identical to the legend of Fig. 20 except the observational estimations. 1) Nguyen et al. (2010). 2) Lacey et al. (2010). 3) Dole et al. (2004) (SDC). 4) Fernandez-Conde et al. (2008). 5) Marsden et al. (2009).

## 5 CONCLUSIONS

In this paper we constructed a model of extragalactic background light and compared it with three other models and with observational data. The primary model, referred to as E2, was based on the eGALICS simulation (Cousin et al. 2015a,b). With help of GRASIL and CHE\_EVO code (Silva et al. 1998) we created the library of SEDs of discs and bulges for a given parameter grid. Each disc or bulge in the eGALICS simulation was assigned an object ID with closest parameters in the SED catalog. The inclination of each galaxy was set random, the AGN contribution and gravitational lensing were taken into account.

We compared this model with a widely used in literature model of Béthermin et al. (2011), referred to as BM in text. We have reproduced source counts using the recipes published in Béthermin et al. (2011). We also compared the results with our previously

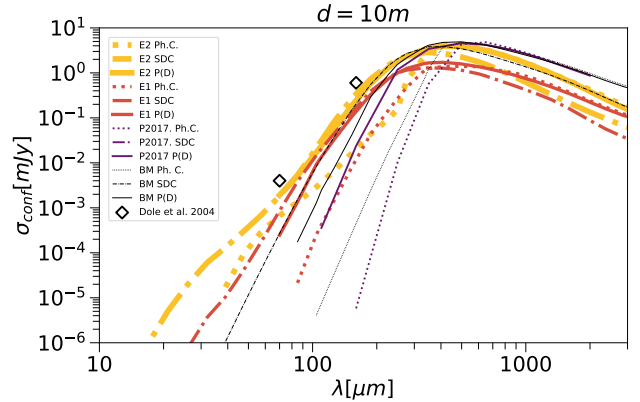


**Figure 22.** Diameter of the main mirror 10 m. The confusion noise vs wavelength for four models considered and three estimation methods. The legend is identical to the legend of Fig. 20 except the observational estimations. 1) Dole et al. (2004) (SDC).

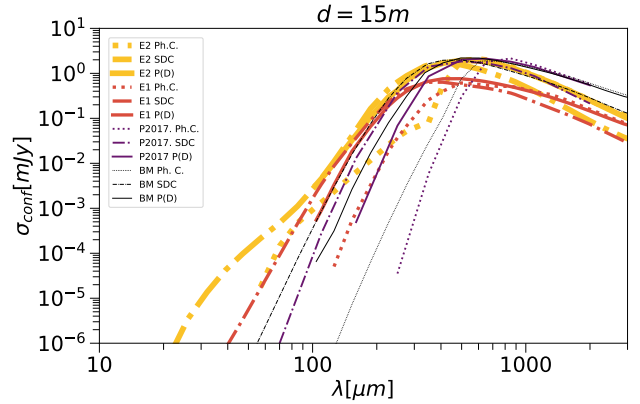


**Figure 23.** Diameter of the main mirror 15 m. The confusion noise vs wavelength for four models considered and three estimation methods. The legend is identical to the legend of Fig. 20 except the observational estimations.

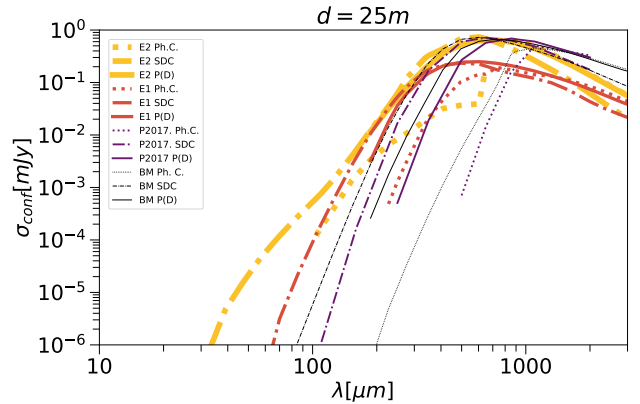


**Figure 24.** Diameter of the main mirror 25 m. The confusion noise vs wavelength for four models considered and three estimation methods. The legend is identical to the legend of Fig. 20 except the observational estimations.

published model (Pilipenko et al. 2017) (P2017). It is based on a simulation of dark matter evolution, mass-luminosity relation and a SED library. The third comparison model (E1) is a simplified one based on the same eGALICS simulation as E2. Only the data on dark matter was used. Then following the approach close but not similar to P2017, we used the  $M - L$  relation and a SED library from Chary & Elbaz (2001), where SED depends solely on luminosity.

With these models we calculated differential and integral number counts, extragalactic background light SEDs for various bins in redshift and luminosity, the dependence of the confusion noise from wavelength and telescope diameter. Models BM, P2017, E2 demonstrate fair agreement with each other and observational data in case such data is available. The main feature of E2 model is the lack of a priori set free parameters, whether BM and P2017 models are in fact very complex approximations of the observational data.

We have analyzed the number counts of sources on a 2D flux-redshift plane. All the models have shown obvious trends: the increase of contribution of distant galaxies on lower fluxes and longer wavelengths. Besides this, the 2D distributions turned to be quite sensitive to the way in which the model is constructed. Simple models based on the mass-luminosity relation show an abrupt dropoff of number counts above some redshift which depends on flux. BM and E2 models show a much more complicated behaviour: for a given flux there may exist multiple peaks of number counts at different redshifts. We believe that these features can be used to further test and constrain models of submillimeter galaxies.

All models reproduce the total background SED fairly well. The same is true for relatively small redshifts:  $0 < z < 1$  and  $1 < z < 2$ . The deviation of the E1 model with all other models can be explained by the SEDs used in it.

If we consider the contribution to EBL from galaxies with different luminosities the following trend can be found. A model based on SEDs assigned to galaxies by the properties of their baryonic matter and a model based on simple  $M - L$  ratio will show similar results for massive haloes and, therefore, high luminosities. For relatively low luminosities  $10^6 L_\odot - 10^8 L_\odot$  the E2 model predicts higher contribution to EBL. That is because the  $M - L$  ratio predicts lower luminosities for low mass objects. The short wavelengths are the most affected.

We used different methods to estimate confusion limits for telescopes with diameters of 0.85 m–25 m on wavelengths 75–2000  $\mu\text{m}$ . It was discussed how the shape of the curve of the source number counts affects the confusion noise estimates. We conclude that simple models, based on the mass-luminosity relation, can be used to reliably predict the confusion noise for Millimetron or other 10-m class telescopes only for wavelengths shorter than 650 microns. For larger wavelengths more sophisticated models are needed. Our new model, based on public eGALICS simulation and GRASIL and CHE\_EVO codes, turned out to be consistent with observational data and allows to explore the confusion limit in the whole range of wavelengths accessible by Millimetron. We have also tested the source counts in optical wavelengths (Appendix B), which may be helpful in testing methods of reducing the confusion noise which use information from multiple bands.

## ACKNOWLEDGEMENTS

This research has made use of the Tool for Operations on catalogs And Tables (TOPCAT; Taylor 2005): [www.starlink.ac.uk/topcat/](http://www.starlink.ac.uk/topcat/);

This research made use of SciPy and NumPy Jones et al. (2001), and the AstroML Vanderplas et al. (2012) package.

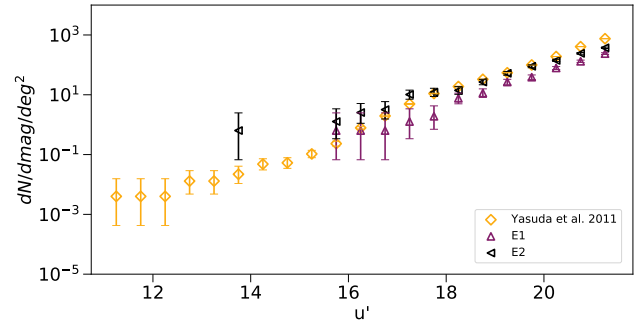


**Figure A1.** Number counts in the SDSS  $u'$  band. 1) SDSS observational data (Yasuda et al. (2001)). 2) E1 model. 3) E2 model.

The work of A.A. Ermash and S.V. Pilipenko was supported by the project N01-2018 of the program ‘The new scientific groups of LPI’. The work of V.N. Lukash was supported by Russian Foundation for Basic Research grant 16-02-01043. This study was supported by the Russian Academy of Science Presidium Fundamental Research program P-28.

## APPENDIX A: SDSS

Despite the fact that optical source counts are outside the scope of this paper they provide a good test of the results obtained. Observational data were taken from Yasuda et al. (2001) where data for four optical bands are given:  $u'$ ,  $g'$ ,  $r'$ ,  $i'$  and  $z'$ .

In order to calculate the magnitudes we need the information about the sensitivity curves, which was taken from <http://www-star.fnal.gov/ugriz/Filters/response.html>. The equation used to calculate the magnitudes in this system is (Smith et al. (2002)):

$$m = -2.5 \log \frac{\int d(\log \nu) f_\nu S_\nu}{\int d(\log \nu) S_\nu} - 48.60 \quad (\text{A1})$$

where  $S_\nu$  is the flux in units  $\text{ergs}^{-1}\text{cm}^{-2}\text{Hz}^{-1}$ ,  $f_\nu$  is the filter response curves.

The counts were calculated for the E1 and E2 models. We have implied the redshift cut  $z < 1.2$  to limit the calculation time. As can be seen from figures A1, A2, A3, A4, A5, both models correspond with each other and the observational data fairly well. The drop off in  $i'$  and  $z'$  on high magnitudes is caused by the limited depth of the survey. Such successful prediction of optical number counts is not surprising. For close objects usage of a SED catalog obtained for local galaxies is a justified assumption. Lensing is also not expected to have any significant influence, nevertheless we included it, just in case. The E2 model does not show advantages in this case except for the  $u'$  band where E2 reproduces the number counts better than E1. This effect is due to the presence of AGN in the former model.

## APPENDIX B: NUMBER COUNTS TABLES

In this appendix in Table B1 source number counts for two models are given. Wavelength  $\lambda = 650\mu\text{m}$ . This is a short example of the data available online

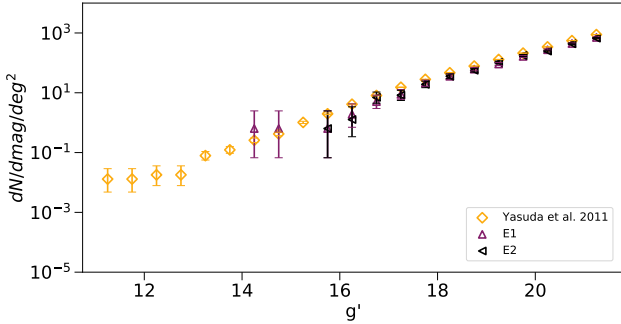


**Figure A2.** Number counts in the SDSS  $g'$  band. Legend is identical to figure A1.

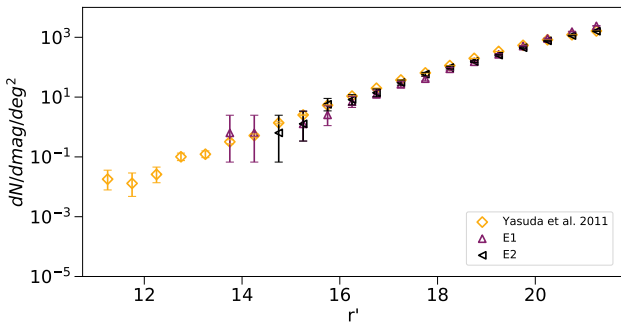


**Figure A3.** Number counts in the SDSS  $r'$  band. Legend is identical to figure A1.

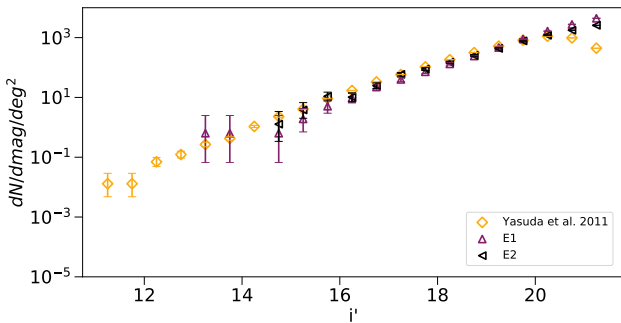


**Figure A4.** Number counts in the SDSS  $i'$  band. Legend is identical to figure A1.

## REFERENCES

- Aguirre P., et al., 2018, *ApJ*, 855, 26  
 Aravena M., et al., 2016, *ApJ*, 833, 68  
 Aretxaga I., et al., 2011, *MNRAS*, 415, 3831  
 Austermann J. E., et al., 2009, *MNRAS*, 393, 1573  
 Austermann J. E., et al., 2010, *MNRAS*, 401, 160  
 Beichman C. A., Neugebauer G., Habing H. J., Clegg P. E., Chester T. J., eds, 1988, Infrared astronomical satellite (IRAS) catalogs and atlases. Volume 1: Explanatory supplement Vol. 1  
 Berta S., et al., 2010, *A&A*, 518, L30  
 Berta S., et al., 2011, *A&A*, 532, A49  
 Béthermin M., Dole H., 2011, preprint, ([arXiv:1102.1827](https://arxiv.org/abs/1102.1827))  
 Béthermin M., Dole H., Beelen A., Aussel H., 2010a, *A&A*, 512, A78  
 Béthermin M., Dole H., Cousin M., Bavouzet N., 2010b, *A&A*, 516, A43  
 Béthermin M., Dole H., Lagache G., Le Borgne D., Penin A., 2011, *Astronomy and Astrophysics*, 529, A4  
 Béthermin M., et al., 2012a, *A&A*, 542, A58  
 Béthermin M., et al., 2012b, *ApJ*, 757, L23  
 Blaizot J., Wadadekar Y., Guiderdoni B., Colombi S. T., Bertin E., Bouchet F. R., Devriendt J. E. G., Hatton S., 2005, *MNRAS*, 360, 159  
 Bouché N., et al., 2010, *ApJ*, 718, 1001  
 Bryan G. L., Norman M. L., 1998, *ApJ*, 495, 80  
 Carniani S., et al., 2015, *A&A*, 584, A78  
 Cattaneo A., Blaizot J., Devriendt J., Guiderdoni B., 2005, *MNRAS*, 364, 407  
 Cattaneo A., Dekel A., Devriendt J., Guiderdoni B., Blaizot J., 2006, *MNRAS*, 370, 1651  
 Chary R., Elbaz D., 2001, *ApJ*, 556, 562  
 Chen C.-C., Cowie L. L., Barger A. J., Casey C. M., Lee N., Sanders D. B., Wang W.-H., Williams J. P., 2013a, *ApJ*, 762, 81  
 Chen C.-C., Cowie L. L., Barger A. J., Casey C. M., Lee N., Sanders D. B., Wang W.-H., Williams J. P., 2013b, *ApJ*, 776, 131  
 Clements D. L., et al., 2010, *A&A*, 518, L8  
 Clements D. L., Bendo G., Pearson C., Khan S. A., Matsuura S., Shirahata M., 2011, *MNRAS*, 411, 373  
 Cole S., Lacey C. G., Baugh C. M., Frenk C. S., 2000, *MNRAS*, 319, 168  
 Conroy C., Wechsler R. H., 2009, *ApJ*, 696, 620  
 Cousin M., Lagache G., Bethermin M., Blaizot J., Guiderdoni B., 2015a, *A&A*, 575, A32  
 Cousin M., Lagache G., Bethermin M., Guiderdoni B., 2015b, *A&A*, 575, A33  
 Croton D. J., et al., 2006, *MNRAS*, 365, 11  
 Devriendt J. E. G., Guiderdoni B., 2000, *A&A*, 363, 851  
 Dole H., Lagache G., Puget J.-L., 2003, *ApJ*, 585, 617  
 Dole H., et al., 2004, *ApJS*, 154, 93  
 Domínguez A., et al., 2011, *MNRAS*, 410, 2556  
 Dwek E., Krennrich F., 2013, *Astroparticle Physics*, 43, 112  
 Fernandez-Conde N., Lagache G., Puget J.-L., Dole H., 2008, *A&A*, 481, 885  
 Fixsen D. J., Dwek E., Mather J. C., Bennett C. L., Shafer R. A., 1998, *ApJ*, 508, 123  
 Franceschini A., Rodighiero G., Vaccari M., Berta S., Marchetti L., Mainetti G., 2010, *A&A*, 517, A74  
 Frayer D. T., et al., 2006, *AJ*, 131, 250  
 Frayer D. T., et al., 2009, *AJ*, 138, 1261  
 Fujimoto S., Ouchi M., Ono Y., Shibuya T., Ishigaki M., Nagai H., Momose R., 2016, *ApJS*, 222, 1  
 Geach J. E., et al., 2017, *MNRAS*, 465, 1789  
 Gehrels N., 1986, *ApJ*, 303, 336  
 Glenn J., et al., 2010, *MNRAS*, 409, 109  
 Granato G. L., De Zotti G., Silva L., Bressan A., Danese L., 2004, *ApJ*, 600, 580  
 Pérez-Sánchez R. B., et al., 2010, *ApJ*, 715, 1020  
 Poglitsch A., et al., 2010, *A&A*, 518, A91  
 Poglitsch A., et al., 2011, *A&A*, 532, A100  
 Poglitsch A., et al., 2012, *A&A*, 542, A101  
 Poglitsch A., et al., 2013, *A&A*, 558, A100  
 Poglitsch A., et al., 2014, *A&A*, 566, A100  
 Poglitsch A., et al., 2015, *A&A*, 584, A100  
 Poglitsch A., et al., 2016, *A&A*, 592, A100  
 Poglitsch A., et al., 2017, *A&A*, 606, A100  
 Poglitsch A., et al., 2018, *A&A*, 616, A100  
 Poglitsch A., et al., 2019, *A&A*, 628, A100  
 Poglitsch A., et al., 2020, *A&A*, 638, A100  
 Poglitsch A., et al., 2021, *A&A*, 648, A100  
 Poglitsch A., et al., 2022, *A&A*, 658, A100  
 Poglitsch A., et al., 2023, *A&A*, 668, A100  
 Poglitsch A., et al., 2024, *A&A*, 678, A100  
 Poglitsch A., et al., 2025, *A&A*, 688, A100  
 Poglitsch A., et al., 2026, *A&A*, 698, A100  
 Poglitsch A., et al., 2027, *A&A*, 708, A100  
 Poglitsch A., et al., 2028, *A&A*, 718, A100  
 Poglitsch A., et al., 2029, *A&A*, 728, A100  
 Poglitsch A., et al., 2030, *A&A*, 738, A100  
 Poglitsch A., et al., 2031, *A&A*, 748, A100  
 Poglitsch A., et al., 2032, *A&A*, 758, A100  
 Poglitsch A., et al., 2033, *A&A*, 768, A100  
 Poglitsch A., et al., 2034, *A&A*, 778, A100  
 Poglitsch A., et al., 2035, *A&A*, 788, A100  
 Poglitsch A., et al., 2036, *A&A*, 798, A100  
 Poglitsch A., et al., 2037, *A&A*, 808, A100  
 Poglitsch A., et al., 2038, *A&A*, 818, A100  
 Poglitsch A., et al., 2039, *A&A*, 828, A100  
 Poglitsch A., et al., 2040, *A&A*, 838, A100  
 Poglitsch A., et al., 2041, *A&A*, 848, A100  
 Poglitsch A., et al., 2042, *A&A*, 858, A100  
 Poglitsch A., et al., 2043, *A&A*, 868, A100  
 Poglitsch A., et al., 2044, *A&A*, 878, A100  
 Poglitsch A., et al., 2045, *A&A*, 888, A100  
 Poglitsch A., et al., 2046, *A&A*, 898, A100  
 Poglitsch A., et al., 2047, *A&A*, 908, A100  
 Poglitsch A., et al., 2048, *A&A*, 918, A100  
 Poglitsch A., et al., 2049, *A&A*, 928, A100  
 Poglitsch A., et al., 2050, *A&A*, 938, A100  
 Poglitsch A., et al., 2051, *A&A*, 948, A100  
 Poglitsch A., et al., 2052, *A&A*, 958, A100  
 Poglitsch A., et al., 2053, *A&A*, 968, A100  
 Poglitsch A., et al., 2054, *A&A*, 978, A100  
 Poglitsch A., et al., 2055, *A&A*, 988, A100  
 Poglitsch A., et al., 2056, *A&A*, 998, A100  
 Poglitsch A., et al., 2057, *A&A*, 1008, A100  
 Poglitsch A., et al., 2058, *A&A*, 1018, A100  
 Poglitsch A., et al., 2059, *A&A*, 1028, A100  
 Poglitsch A., et al., 2060, *A&A*, 1038, A100  
 Poglitsch A., et al., 2061, *A&A*, 1048, A100  
 Poglitsch A., et al., 2062, *A&A*, 1058, A100  
 Poglitsch A., et al., 2063, *A&A*, 1068, A100  
 Poglitsch A., et al., 2064, *A&A*, 1078, A100  
 Poglitsch A., et al., 2065, *A&A*, 1088, A100  
 Poglitsch A., et al., 2066, *A&A*, 1098, A100  
 Poglitsch A., et al., 2067, *A&A*, 1108, A100  
 Poglitsch A., et al., 2068, *A&A*, 1118, A100  
 Poglitsch A., et al., 2069, *A&A*, 1128, A100  
 Poglitsch A., et al., 2070, *A&A*, 1138, A100  
 Poglitsch A., et al., 2071, *A&A*, 1148, A100  
 Poglitsch A., et al., 2072, *A&A*, 1158, A100  
 Poglitsch A., et al., 2073, *A&A*, 1168, A100  
 Poglitsch A., et al., 2074, *A&A*, 1178, A100  
 Poglitsch A., et al., 2075, *A&A*, 1188, A100  
 Poglitsch A., et al., 2076, *A&A*, 1198, A100  
 Poglitsch A., et al., 2077, *A&A*, 1208, A100  
 Poglitsch A., et al., 2078, *A&A*, 1218, A100  
 Poglitsch A., et al., 2079, *A&A*, 1228, A100  
 Poglitsch A., et al., 2080, *A&A*, 1238, A100  
 Poglitsch A., et al., 2081, *A&A*, 1248, A100  
 Poglitsch A., et al., 2082, *A&A*, 1258, A100  
 Poglitsch A., et al., 2083, *A&A*, 1268, A100  
 Poglitsch A., et al., 2084, *A&A*, 1278, A100  
 Poglitsch A., et al., 2085, *A&A*, 1288, A100  
 Poglitsch A., et al., 2086, *A&A*, 1298, A100  
 Poglitsch A., et al., 2087, *A&A*, 1308, A100  
 Poglitsch A., et al., 2088, *A&A*, 1318, A100  
 Poglitsch A., et al., 2089, *A&A*, 1328, A100  
 Poglitsch A., et al., 2090, *A&A*, 1338, A100  
 Poglitsch A., et al., 2091, *A&A*, 1348, A100  
 Poglitsch A., et al., 2092, *A&A*, 1358, A100  
 Poglitsch A., et al., 2093, *A&A*, 1368, A100  
 Poglitsch A., et al., 2094, *A&A*, 1378, A100  
 Poglitsch A., et al., 2095, *A&A*, 1388, A100  
 Poglitsch A., et al., 2096, *A&A*, 1398, A100  
 Poglitsch A., et al., 2097, *A&A*, 1408, A100  
 Poglitsch A., et al., 2098, *A&A*, 1418, A100  
 Poglitsch A., et al., 2099, *A&A*, 1428, A100  
 Poglitsch A., et al., 2010, *A&A*, 518, L30  
 Poglitsch A., et al., 2011, *A&A*, 532, A49  
 Poglitsch A., et al., 2012, *A&A*, 542, A58  
 Poglitsch A., et al., 2013, *A&A*, 558, A100  
 Poglitsch A., et al., 2014, *A&A*, 572, A100  
 Poglitsch A., et al., 2015, *A&A*, 586, A100  
 Poglitsch A., et al., 2016, *A&A*, 598, A100  
 Poglitsch A., et al., 2017, *A&A*, 610, A100  
 Poglitsch A., et al., 2018, *A&A*, 622, A100  
 Poglitsch A., et al., 2019, *A&A*, 634, A100  
 Poglitsch A., et al., 2020, *A&A*, 646, A100  
 Poglitsch A., et al., 2021, *A&A*, 658, A100  
 Poglitsch A., et al., 2022, *A&A*, 670, A100  
 Poglitsch A., et al., 2023, *A&A*, 682, A100  
 Poglitsch A., et al., 2024, *A&A*, 694, A100  
 Poglitsch A., et al., 2025, *A&A*, 706, A100  
 Poglitsch A., et al., 2026, *A&A*, 718, A100  
 Poglitsch A., et al., 2027, *A&A*, 730, A100  
 Poglitsch A., et al., 2028, *A&A*, 742, A100  
 Poglitsch A., et al., 2029, *A&A*, 754, A100  
 Poglitsch A., et al., 2030, *A&A*, 766, A100  
 Poglitsch A., et al., 2031, *A&A*, 778, A100  
 Poglitsch A., et al., 2032, *A&A*, 790, A100  
 Poglitsch A., et al., 2033, *A&A*, 802, A100  
 Poglitsch A., et al., 2034, *A&A*, 814, A100  
 Poglitsch A., et al., 2035, *A&A*, 826, A100  
 Poglitsch A., et al., 2036, *A&A*, 838, A100  
 Poglitsch A., et al., 2037, *A&A*, 850, A100  
 Poglitsch A., et al., 2038, *A&A*, 862, A100  
 Poglitsch A., et al., 2039, *A&A*, 874, A100  
 Poglitsch A., et al., 2040, *A&A*, 886, A100  
 Poglitsch A., et al., 2041, *A&A*, 898, A100  
 Poglitsch A., et al., 2042, *A&A*, 910, A100  
 Poglitsch A., et al., 2043, *A&A*, 922, A100  
 Poglitsch A., et al., 2044, *A&A*, 934, A100  
 Poglitsch A., et al., 2045, *A&A*, 946, A100  
 Poglitsch A., et al., 2046, *A&A*, 958, A100  
 Poglitsch A., et al., 2047, *A&A*, 970, A100  
 Poglitsch A., et al., 2048, *A&A*, 982, A100  
 Poglitsch A., et al., 2049, *A&A*, 994, A100  
 Poglitsch A., et al., 2050, *A&A*, 1006, A100  
 Poglitsch A., et al., 2051, *A&A*, 1018, A100  
 Poglitsch A., et al., 2052, *A&A*, 1030, A100  
 Poglitsch A., et al., 2053, *A&A*, 1042, A100  
 Poglitsch A., et al., 2054, *A&A*, 1054, A100  
 Poglitsch A., et al., 2055, *A&A*, 1066, A100  
 Poglitsch A., et al., 2056, *A&A*, 1078, A100  
 Poglitsch A., et al., 2057, *A&A*, 1090, A100  
 Poglitsch A., et al., 2058, *A&A*, 1102, A100  
 Poglitsch A., et al., 2059, *A&A*, 1114, A100  
 Poglitsch A., et al., 2060, *A&A*, 1126, A100  
 Poglitsch A., et al., 2061, *A&A*, 1138, A100  
 Poglitsch A., et al., 2062, *A&A*, 1150, A100  
 Poglitsch A., et al., 2063, *A&A*, 1162, A100  
 Poglitsch A., et al., 2064, *A&A*, 1174, A100  
 Poglitsch A., et al., 2065, *A&A*, 1186, A100  
 Poglitsch A., et al., 2066, *A&A*, 1198, A100  
 Poglitsch A., et al., 2067, *A&A*, 1210, A100  
 Poglitsch A., et al., 2068, *A&A*, 1222, A100  
 Poglitsch A., et al., 2069, *A&A*, 1234, A100  
 Poglitsch A., et al., 2070, *A&A*, 1246, A100  
 Poglitsch A., et al., 2071, *A&A*, 1258, A100  
 Poglitsch A., et al., 2072, *A&A*, 1270, A100  
 Poglitsch A., et al., 2073, *A&A*, 1282, A100  
 Poglitsch A., et al., 2074, *A&A*, 1294, A100  
 Poglitsch A., et al., 2075, *A&A*, 1306, A100  
 Poglitsch A., et al., 2076, *A&A*, 1318, A100  
 Poglitsch A., et al., 2077, *A&A*, 1330, A100  
 Poglitsch A., et al., 2078, *A&A*, 1342, A100  
 Poglitsch A., et al., 2079, *A&A*, 1354, A100  
 Poglitsch A., et al., 2080, *A&A*, 1366, A100  
 Poglitsch A., et al., 2081, *A&A*, 1378, A100  
 Poglitsch A., et al., 2082, *A&A*, 1390, A100  
 Poglitsch A., et al., 2083, *A&A*, 1402, A100  
 Poglitsch A., et al., 2084, *A&A*, 1414, A100  
 Poglitsch A., et al., 2085, *A&A*, 1426, A100  
 Poglitsch A., et al., 2086, *A&A*, 1438, A100  
 Poglitsch A., et al., 2087, *A&A*, 1450, A100  
 Poglitsch A., et al., 2088, *A&A*, 1462, A100  
 Poglitsch A., et al., 2089, *A&A*, 1474, A100  
 Poglitsch A., et al., 2090, *A&A*, 1486, A100  
 Poglitsch A., et al., 2091, *A&A*, 1498, A100  
 Poglitsch A., et al., 2092, *A&A*, 1510, A100  
 Poglitsch A., et al., 2093, *A&A*, 1522, A100  
 Poglitsch A., et al., 2094, *A&A*, 1534, A100  
 Poglitsch A., et al., 2095, *A&A*, 1546, A100  
 Poglitsch A., et al., 2096, *A&A*, 1558, A100  
 Poglitsch A., et al., 2097, *A&A*, 1570, A100  
 Poglitsch A., et al., 2098, *A&A*, 1582, A100  
 Poglitsch A., et al., 2099, *A&A*, 1594, A100  
 Poglitsch A., et al., 2010, *A&A*, 518, L30  
 Poglitsch A., et al., 2011, *A&A*, 532, A49  
 Poglitsch A., et al., 2012, *A&A*, 542, A58  
 Poglitsch A., et al., 2013, *A&A*, 558, A100  
 Poglitsch A., et al., 2014, *A&A*, 572, A100  
 Poglitsch A., et al., 2015, *A&A*, 586, A100  
 Poglitsch A., et al., 2016, *A&A*, 598, A100  
 Poglitsch A., et al., 2017, *A&A*, 610, A100  
 Poglitsch A., et al., 2018, *A&A*, 622, A100  
 Poglitsch A., et al., 2019, *A&A*, 634, A100  
 Poglitsch A., et al., 2020, *A&A*, 646, A100  
 Poglitsch A., et al., 2021, *A&A*, 658, A100  
 Poglitsch A., et al., 2022, *A&A*, 670, A100  
 Poglitsch A., et al., 2023, *A&A*, 682, A100  
 Poglitsch A., et al., 2024, *A&A*, 694, A100  
 Poglitsch A., et al., 2025, *A&A*, 706, A100  
 Poglitsch A., et al., 2026, *A&A*, 718, A100  
 Poglitsch A., et al., 2027, *A&A*, 730, A100  
 Poglitsch A., et al., 2028, *A&A*, 742, A100  
 Poglitsch A., et al., 2029, *A&A*, 754, A100  
 Poglitsch A., et al., 2030, *A&A*, 766, A100  
 Poglitsch A., et al., 2031, *A&A*, 778, A100  
 Poglitsch A., et al., 2032, *A&A*, 790, A100  
 Poglitsch A., et al., 2033, *A&A*, 802, A100  
 Poglitsch A., et al., 2034, *A&A*, 814, A100  
 Poglitsch A., et al., 2035, *A&A*, 826, A100  
 Poglitsch A., et al., 2036, *A&A*, 838, A100  
 Poglitsch A., et al., 2037, *A&A*, 850, A100  
 Poglitsch A., et al., 2038, *A&A*, 862, A100  
 Poglitsch A., et al., 2039, *A&A*, 874, A100  
 Poglitsch A., et al., 2040, *A&A*, 886, A100  
 Poglitsch A., et al., 2041, *A&A*, 898, A100  
 Poglitsch A., et al., 2042, *A&A*, 910, A100  
 Poglitsch A., et al., 2043, *A&A*, 922, A100  
 Poglitsch A., et al., 2044, *A&A*, 934, A100  
 Poglitsch A., et al., 2045, *A&A*, 946, A100  
 Poglitsch A., et al., 2046, *A&A*, 958, A100  
 Poglitsch A., et al., 2047, *A&A*, 970, A100  
 Poglitsch A., et al., 2048, *A&A*, 982, A100  
 Poglitsch A., et al., 2049, *A&A*, 994, A100  
 Poglitsch A., et al., 2050, *A&A*, 1006, A100  
 Poglitsch A., et al., 2051, *A&A*, 1018, A100  
 Poglitsch A., et al., 2052, *A&A*, 1030, A100  
 Poglitsch A., et al., 2053, *A&A*, 1042, A100  
 Poglitsch A., et al., 2054, *A&A*, 1054, A100  
 Poglitsch A., et al., 2055, *A&A*, 1066, A100  
 Poglitsch A., et al., 2056, *A&A*, 1078, A100  
 Poglitsch A., et al., 2057, *A&A*, 1090, A100  
 Poglitsch A., et al., 2058, *A&A*, 1102, A100  
 Poglitsch A., et al., 2059, *A&A*, 1114, A100  
 Poglitsch A., et al., 2060, *A&A*, 1126, A100  
 Poglitsch A., et al., 2061, *A&A*, 1138, A100  
 Poglitsch A., et al., 2062, *A&A*, 1150, A100  
 Poglitsch A., et al., 2063, *A&A*, 1162, A100  
 Poglitsch A., et al.,

**Table B1.** Numerical values of the differential source number counts for  $650\mu\text{m}$ . Tables for another wavelengths for all four models considered are available online.

650 $\mu\text{m}$		
$S_\nu[\text{mJy}]$	P2017	E2
$1.01 \times 10^{-3}$	$2.27^{+0.02}_{-0.02} \times 10^{-1}$	$2.74^{+0.00}_{-0.00} \times 10^0$
$1.43 \times 10^{-3}$	$3.64^{+0.03}_{-0.03} \times 10^{-1}$	$2.73^{+0.00}_{-0.00} \times 10^0$
$2.03 \times 10^{-3}$	$5.84^{+0.05}_{-0.05} \times 10^{-1}$	$2.22^{+0.01}_{-0.01} \times 10^0$
$2.86 \times 10^{-3}$	$9.24^{+0.08}_{-0.08} \times 10^{-1}$	$3.71^{+0.01}_{-0.01} \times 10^0$
$4.04 \times 10^{-3}$	$1.44^{+0.01}_{-0.01} \times 10^0$	$4.51^{+0.01}_{-0.01} \times 10^0$
$5.71 \times 10^{-3}$	$2.34^{+0.02}_{-0.02} \times 10^0$	$8.84^{+0.02}_{-0.02} \times 10^0$
$8.06 \times 10^{-3}$	$3.67^{+0.04}_{-0.04} \times 10^0$	$1.01^{+0.01}_{-0.00} \times 10^1$
$1.14 \times 10^{-2}$	$5.85^{+0.06}_{-0.06} \times 10^0$	$1.12^{+0.01}_{-0.00} \times 10^1$
$1.61 \times 10^{-2}$	$9.09^{+0.10}_{-0.10} \times 10^0$	$1.38^{+0.01}_{-0.01} \times 10^1$
$2.27 \times 10^{-2}$	$1.44^{+0.02}_{-0.02} \times 10^1$	$1.18^{+0.01}_{-0.01} \times 10^1$
$3.21 \times 10^{-2}$	$2.26^{+0.03}_{-0.03} \times 10^1$	$2.35^{+0.01}_{-0.01} \times 10^1$
$4.53 \times 10^{-2}$	$3.61^{+0.04}_{-0.04} \times 10^1$	$4.59^{+0.03}_{-0.03} \times 10^1$
$6.40 \times 10^{-2}$	$5.71^{+0.07}_{-0.07} \times 10^1$	$1.06^{+0.01}_{-0.01} \times 10^2$
$9.05 \times 10^{-2}$	$8.95^{+0.11}_{-0.11} \times 10^1$	$1.71^{+0.01}_{-0.01} \times 10^2$
$1.28 \times 10^{-1}$	$1.40^{+0.02}_{-0.02} \times 10^2$	$2.45^{+0.01}_{-0.01} \times 10^2$
$1.80 \times 10^{-1}$	$2.19^{+0.03}_{-0.03} \times 10^2$	$3.14^{+0.02}_{-0.02} \times 10^2$
$2.55 \times 10^{-1}$	$3.46^{+0.05}_{-0.05} \times 10^2$	$3.03^{+0.03}_{-0.02} \times 10^2$
$3.60 \times 10^{-1}$	$5.51^{+0.08}_{-0.08} \times 10^2$	$5.84^{+0.05}_{-0.04} \times 10^2$
$5.09 \times 10^{-1}$	$9.42^{+0.13}_{-0.13} \times 10^2$	$1.12^{+0.01}_{-0.01} \times 10^3$
$7.19 \times 10^{-1}$	$1.57^{+0.02}_{-0.02} \times 10^3$	$2.63^{+0.02}_{-0.02} \times 10^3$
$1.01 \times 10^0$	$2.05^{+0.03}_{-0.03} \times 10^3$	$2.57^{+0.02}_{-0.02} \times 10^3$
$1.43 \times 10^0$	$2.54^{+0.05}_{-0.05} \times 10^3$	$2.43^{+0.03}_{-0.03} \times 10^3$
$2.03 \times 10^0$	$3.14^{+0.07}_{-0.07} \times 10^3$	$1.49^{+0.03}_{-0.03} \times 10^3$
$2.86 \times 10^0$	$4.06^{+0.10}_{-0.10} \times 10^3$	$6.49^{+0.22}_{-0.22} \times 10^2$
$4.04 \times 10^0$	$4.32^{+0.14}_{-0.13} \times 10^3$	$5.12^{+0.27}_{-0.26} \times 10^2$
$5.71 \times 10^0$	$1.39^{+0.10}_{-0.10} \times 10^3$	$5.47^{+0.36}_{-0.34} \times 10^2$
$8.06 \times 10^0$	$9.45^{+0.13}_{-0.13} \times 10^2$	$5.66^{+0.48}_{-0.45} \times 10^2$
$1.14 \times 10^1$	$8.17^{+1.40}_{-1.22} \times 10^2$	$1.09^{+0.08}_{-0.08} \times 10^3$
$1.61 \times 10^1$	$6.27^{+1.68}_{-1.33} \times 10^2$	$5.98^{+0.86}_{-0.77} \times 10^2$
$2.27 \times 10^1$	$1.64^{+1.31}_{-0.84} \times 10^2$	$3.35^{+0.90}_{-0.73} \times 10^2$
$3.21 \times 10^1$	$2.21^{+2.20}_{-1.24} \times 10^2$	$1.58^{+0.91}_{-0.63} \times 10^2$
$4.53 \times 10^1$	$1.85^{+3.08}_{-1.36} \times 10^2$	$2.36^{+1.47}_{-0.99} \times 10^2$
$6.40 \times 10^1$	$1.56^{+4.50}_{-1.39} \times 10^2$	$1.49^{+1.82}_{-0.94} \times 10^2$

- Gruppioni C., Pozzi F., Zamorani G., Vignali C., 2011, *MNRAS*, **416**, 70  
 Guideroni B., Hivon E., Bouchet F. R., Maffei B., 1998, *MNRAS*, **295**, 877  
 Guo Q., et al., 2011, *MNRAS*, **413**, 101  
 Hatsukade B., et al., 2011, *MNRAS*, **411**, 102  
 Hatsukade B., Ohta K., Seko A., Yabe K., Akiyama M., 2013, *ApJ*, **769**, L27  
 Hatsukade B., et al., 2016, *PASJ*, **68**, 36  
 Hayward C. C., Narayanan D., Kereš D., Jonsson P., Hopkins P. F., Cox T. J., Hernquist L., 2013, *MNRAS*, **428**, 2529  
 Henriques B. M. B., White S. D. M., Thomas P. A., Angulo R. E., Guo Q., Lemson G., Springel V., 2013, *MNRAS*, **431**, 3373  
 Hopkins P. F., Hernquist L., Cox T. J., Kereš D., 2008a, *ApJS*, **175**, 356  
 Hopkins P. F., Cox T. J., Kereš D., Hernquist L., 2008b, *ApJS*, **175**, 390  
 Hopkins P. F., Younger J. D., Hayward C. C., Narayanan D., Hernquist L., 2010, *MNRAS*, **402**, 1693  
 Hsu L.-Y., Cowie L. L., Chen C.-C., Barger A. J., Wang W.-H., 2016, *ApJ*, **829**, 25  
 Ilić S., Blanchard A., Douspis M., 2015, *A&A*, **582**, A79  
 Jeong W.-S., Pearson C. P., Lee H. M., Pak S., Nakagawa T., 2006, *MNRAS*, **369**, 281  
 Johansson D., Sigurdarson H., Horellou C., 2011, *A&A*, **527**, A117  
 Jones E., Oliphant T., Peterson P., et al., 2001, SciPy: Open source scientific tools for Python, <http://www.scipy.org/>  
 Kardashev N. S., 2017, *Astronomy Reports*, **61**, 310  
 Kardashev N. S., et al., 2014, *Physics Uspekhi*, **57**, 1199  
 Karim A., et al., 2013, *MNRAS*, **432**, 2  
 Kim S.-H., Takemasa K.-i., Takeuchi Y., Matsuura S., 2012, *Journal of the Physical Society of Japan*, **81**, 024101  
 Klypin A., Yepes G., Gottlöber S., Prada F., Heß S., 2016, *MNRAS*, **457**, 4340  
 Lacey C. G., Baugh C. M., Frenk C. S., Benson A. J., Orsi A., Silva L., Granato G. L., Bressan A., 2010, *MNRAS*, **405**, 2  
 Lagache G., Dole H., Puget J.-L., 2003, *MNRAS*, **338**, 555  
 Landy S. D., Szalay A. S., 1993, *ApJ*, **412**, 64  
 Larson D., et al., 2011, *ApJS*, **192**, 16  
 Le Borgne D., Elbaz D., Ocvirk P., Pichon C., 2009, *A&A*, **504**, 727  
 Lyu J., Rieke G. H., 2017, *ApJ*, **841**, 76  
 Magnelli B., et al., 2013, *A&A*, **553**, A132  
 Marsden G., et al., 2009, *ApJ*, **707**, 1729  
 Marsden G., et al., 2011, *MNRAS*, **417**, 1192  
 Men'shchikov A., 2013, *A&A*, **560**, A63  
 Men'shchikov A., 2017, *A&A*, **607**, A64  
 Men'shchikov A., André P., Didelon P., Motte F., Hennemann M., Schneider N., 2012, *A&A*, **542**, A81  
 Michałowski M., Hjorth J., Watson D., 2010, *A&A*, **514**, A67  
 Mocanu L. M., et al., 2013, *ApJ*, **779**, 61  
 Monaco P., Fontanot F., Taffoni G., 2007, *MNRAS*, **375**, 1189  
 Muñoz Arancibia A. M., et al., 2017, preprint, ([arXiv:1712.03983](https://arxiv.org/abs/1712.03983))  
 Murakami H., et al., 2007, *PASJ*, **59**, S369  
 Nguyen H. T., et al., 2010, *A&A*, **518**, L5  
 Noble A. G., et al., 2012, *MNRAS*, **419**, 1983  
 Oliver S. J., et al., 2010, *A&A*, **518**, L21  
 Ono Y., Ouchi M., Kurono Y., Momose R., 2014, *ApJ*, **795**, 5  
 Oteo I., Zwaan M. A., Ivison R. J., Smail I., Biggs A. D., 2016, *ApJ*, **822**, 36  
 Patanchon G., et al., 2009, *ApJ*, **707**, 1750  
 Pearson C. P., 2001, *MNRAS*, **325**, 1511  
 Perrotta F., Baccigalupi C., Bartelmann M., De Zotti G., Granato G. L., 2001, ArXiv Astrophysics e-prints,  
 Perrotta F., Baccigalupi C., Bartelmann M., De Zotti G., Granato G. L., 2002, *MNRAS*, **329**, 445  
 Pilipenko S. V., Tkachev M. V., Ermash A. A., Larchenkova T. I., Mikheeva E. V., Lukash V. N., 2017, *Astronomy Letters*, **43**, 644  
 Planck Collaboration et al., 2013, *A&A*, **550**, A133  
 Planck Collaboration et al., 2014, *A&A*, **571**, A30  
 Rahmati A., van der Werf P. P., 2011, *MNRAS*, **418**, 176  
 Raymond G., Isaak K. G., Clements D., Rykala A., Pearson C., 2010, *PASJ*, **62**, 697  
 Reed D. S., Bower R., Frenk C. S., Jenkins A., Theuns T., 2007, *MNRAS*, **374**, 2  
 Rieke G. H., et al., 2004, *ApJS*, **154**, 25  
 Risaliti G., Elvis M., 2004, in Barger A. J., ed., *Astrophysics and Space Science Library* Vol. 308, *Supermassive Black Holes in the Distant Universe*. p. 187 ([arXiv:astro-ph/0403618](https://arxiv.org/abs/astro-ph/0403618)), doi:10.1007/978-1-4020-2471-9\_6  
 Roche N., Eales S. A., 1999, *MNRAS*, **307**, 111  
 Rosati P., Borgani S., Norman C., 2002, *ARA&A*, **40**, 539  
 Rowan-Robinson M., 2009, *MNRAS*, **394**, 117  
 Safarzadeh M., et al., 2014, in American Astronomical Society Meeting Abstracts #223. p. 433.06  
 Schneider P., Ehlers J., Falco E. E., 1992, *Gravitational Lenses*, doi:10.1007/978-3-662-03758-4.  
 Scott K. S., et al., 2010, *MNRAS*, **405**, 2260  
 Scott K. S., et al., 2012, *MNRAS*, **423**, 575  
 Silva L., Granato G. L., Bressan A., Danese L., 1998, *ApJ*, **509**, 103  
 Simpson J. M., et al., 2015, *ApJ*, **807**, 128  
 Siringo G., et al., 2009, *A&A*, **497**, 945  
 Siringo G., et al., 2010, *The Messenger*, **139**, 20  
 Smirnov A. V., et al., 2012, in *Space Telescopes and Instrumentation 2012: Optical, Infrared, and Millimeter Wave*. p. 84424C, doi:10.1117/12.927184

- Smith J. A., et al., 2002, [AJ](#), **123**, 2121  
 Somerville R. S., Hopkins P. F., Cox T. J., Robertson B. E., Hernquist L.,  
 2008, [MNRAS](#), **391**, 481  
 Stach S. M., et al., 2018, [ApJ](#), **860**, 161  
 Takeuchi T. T., Ishii T. T., Hirashita H., Yoshikawa K., Matsuhara H., Kawara  
 K., Okuda H., 2001, [PASJ](#), **53**, 37  
 Tan J. C., Silk J., Balland C., 1999, [ApJ](#), **522**, 579  
 Umehata H., et al., 2017, [ApJ](#), **835**, 98  
 Valiante E., Lutz D., Sturm E., Genzel R., Chapin E. L., 2009, [ApJ](#), **701**,  
 1814  
 Valiante E., et al., 2010, [ApJS](#), **191**, 222  
 Valiante E., et al., 2016, [MNRAS](#), **462**, 3146  
 Vanderplas J., Connolly A., Ivezić Ž., Gray A., 2012, in Conference on Intelligent Data Understanding (CIDU). pp 47 –54,  
 doi:10.1109/CIDU.2012.6382200  
 Vieira J. D., et al., 2010, [ApJ](#), **719**, 763  
 Viero M. P., et al., 2013, [ApJ](#), **779**, 32  
 Wang Y. P., 2002, [A&A](#), **383**, 755  
 Wang Y. P., Biermann P. L., 2000, [A&A](#), **356**, 808  
 Weinmann S. M., Pasquali A., Oppenheimer B. D., Finlator K., Mendel J. T.,  
 Crain R. A., Macciò A. V., 2012, [MNRAS](#), **426**, 2797  
 Wilman R. J., et al., 2008, [MNRAS](#), **388**, 1335  
 Wilman R. J., Jarvis M. J., Mauch T., Rawlings S., Hickey S., 2010, [MNRAS](#),  
 405, 447  
 Wilson G. W., et al., 2008, [MNRAS](#), **386**, 807  
 Wu H.-Y., Doré O., 2017, [MNRAS](#), **467**, 4150  
 Yasuda N., et al., 2001, [AJ](#), **122**, 1104  
 Younger J. D., Hopkins P. F., 2011, [MNRAS](#), **410**, 2180  
 Zavala J. A., et al., 2017, [MNRAS](#), **464**, 3369  
 Zeballos M., et al., 2018, [MNRAS](#), **479**, 4577  
 Zemcov M., Blain A., Halpern M., Levenson L., 2010, [ApJ](#), **721**, 424

This paper has been typeset from a  $\text{\TeX}$ / $\text{\LaTeX}$  file prepared by the author.